Advances in Microscale Droplet Generation and Manipulation

Rutvik Lathia[1], Krishnadas Narayanan Nampoothiri[1,2], Nitish Sagar[1], Shubhi Bansal[1,3], Chandantaru Dey Modak[1,4] and Prosenjit Sen[1,*]

[1]Centre for Nano Science and Engineesring, Indian Institute of Science, Bangalore – 560012, India
[2]Department of Mechanical Engineering, Amrita School of Engineering, Amrita Vishwa Vidyapeetham, Chennai – 601103, India
[3]University College London, London WC1E 6BT, U.K.
[4]Laboratoire de Biophysique et Evolution, UMR CNRS-ESPCI 8231 Chimie Biologie Innovation, PSL University, ESPCI Paris, 10 rue Vauquelin, 75005 Paris, France

*Corresponding Author, Email: prosenjits@iisc.ac.in

Abstract

Microscale droplet generation and manipulation have widespread applications in numerous fields, from biochemical assays to printing and additive manufacturing. There are several techniques for droplet handling. Most techniques, however, can generate and work with only a limited range of droplet sizes. Further, there are constraints regarding the workable variety of fluid properties (e.g., viscosity, surface tension, mass loading, etc.). Recent works have focused on developing techniques to overcome these limitations. This review discusses advances in this area that cover a wide range of droplet sizes from sub-picolitre to microliters.

Introduction

Precise generation and manipulation of small droplets remain attractive due to their applications in many domains. Generation of these droplets is of significant interest in the field of aerosol formation,[1,2] chemistry for performing chemical reactions,[3,4] micro/nanoparticle synthesis,[5,6] thermal management for cooling electronic devices,[7,8] and as pathogen carriers in biology.[9,10] However, the generation and manipulation of droplets less than the capillary length scale always remain challenging. This is because of the domination of surface tension force at such a length scale, which limits the droplet size.[11] In order to eject smaller droplets (< 2.5mm), the surface tension force is overcome by applying external forces.[11] Based on this principle, different droplet generation techniques have been developed. While the basic principle remains the same, the distinction between different techniques is based on the nature of the force.[12]

Microfluidics has been employed for the generation of droplets. Various techniques such as crossflow, co-flow, flow-focusing, magnetic and centrifugal force have been explored widely in past literature for microfluidics-based droplet generation.[13,14] The crossflow geometry refers to when two streams of the fluid meet at a certain angle, while in co-flow geometry, two flows are parallel to each other. In flow-focusing microfluidics devices, flows are hydrodynamically focused via contraction. In such devices, droplet generation happens through various breakup modes such as squeezing, dripping, jetting, and tip streaming.[13,15] Droplet breakup can also be reversibly turned on and off by external forces such as acoustics.[16] There has been a plethora of good review literature on microfluidic approaches of droplet generation.[13,17–20]

Another way of droplet generation is based on pushing fluid through a confined nozzle using impulsive forces. These forces act in the vicinity of the fluid interface to eject single droplets. The source can be piezo,[11,12] thermal,[21] acoustic,[22] and electric forces.[23] The applied force causes a localized pressure pulse which pushes the fluid through the nozzle to eject a single drop.[12,24] Based on ink types or applications, different techniques find their use.[25] Techniques such as electrohydrodynamic (EHD) printing uses DC and kHz AC electric fields to generate micron-sized polar and conductive droplets. Such a technique is extremely useful in printing high viscous (~ 1000 mPa.s) and intermediate mass loading (~ 30%) inks with minimum nozzle clogging issues and high resolution compared to inkjet printers. EHD and aerosol jet printing are preferred for electronic circuits due to the requirement for high resolution. However, the EHD printing technique is not used for biological-based inks.[23] The cells are exposed to a high electric field, which decreases their viability.[26] In some cases, the high shear rate also reduces cell viability.[27] Hence, for biobased applications, piezo-based inkjet printing is recommended. Similar high-viscosity inks are also handled using acoustophoretic printing.[22] Regardless of optimizing the inks,[28] most techniques are constrained in their capability to handle a wide variety of fluid properties and droplet sizes.[29] The detailed comparison of the printing technologies is given in Table 1.

Droplet generation and manipulation across scales are desirable for many critical applications. For example, micron-sized droplets are essential in printing applications. Droplets in the 10's to several 100's micron sizes are used in single-cell analysis and material jetting. Techniques in this regime range are primarily nozzle based.[11,12] Further reduction in droplet size is a challenging task because of the limitation in reducing nozzle size. To address these limitations, some new approaches, such as electrochemical and pyroelectrohydrodynamic shooting, have

been explored for dispensing nano-pico-sized droplets.[30,31] In an electrochemical-based approach, the electric field was applied on a macroscopic droplet resting on a copper wire to disperse it into tiny droplets. The electric field helps in overcoming the huge energy gap between macroscopic and corresponding dispersed droplets. At the same time, nanostructured copper wire helps in promoting the splitting of liquid bridges. In pyroelectrohydrodynamic shooting, the electric field is generated by local pyroelectric forces. Such forces were activated by scanning a hot tip or an infrared laser over a lithium niobate substrate. Owing to low power requirements and robust fabrication methods, surface acoustic waves (SAW) based techniques are preferred for atomizing micron-sized (picoliter) droplets.[32,33] Nevertheless, this technique is expensive due to the necessity of a piezoelectric substrate like Lithium Niobate (LiNbO3)[34] or thin-film Zinc Oxide (ZnO).[35]

Generation and manipulation of larger millimeter-sized (microliter) droplets are essential for many biomedical applications.[36–39] In this size range digital microfluidic devices using electric fields are appealing due to their simple design and capability to work with small sample volumes.[40,41] The manipulation of the millimetric-size droplet is usually performed through various electric and magnetic platforms.[42,43] Droplet actuation using DC or low frequency (Hz) electric fields on dielectric-coated electrodes is termed Electrowetting on Dielectric (EWOD).[42] Electrowetting has been explored for multiple applications because it enables programmability, reconfigurability, and realization of portable handheld systems.[44] It is also being used in emerging application spaces like microfluidic acoustic metamaterial.[45] Electrowetting-based manipulation also allows operations like droplet generation, oscillation,[46,47] merging,[48] splitting,[49] bouncing,[50] and mixing.[51] Additionally, spontaneous charging of the droplet has also been utilized for droplet manipulation applications. Optical manipulation of the droplets has also been reported in the literature; however, it is mostly dependent on the substrate properties.[52–54] Additionally, thermal Marangoni-based propulsion is also reported for droplet manipulation. Besides these, droplet impact and manipulation over various wettable surfaces also find their application in various areas such as anti-icing, electricity generation, dispensing, energy harvesting, spraying, heat transfer, self-cleaning, and low hysteresis surfaces.[55,56]

Despite several advances, many challenges still exist in droplet generation and manipulation. Some of these challenges have arisen due to new applications such as 3D printing, rapid manufacturing, and bio-printing. This paper reviews works which attempt to address these unique challenges by developing new techniques. We look at a technique to generate sub-

picolitre volume droplets. This technique is enabled by directly heating larger droplets to create a vapor field. Then charge-induced condensation is used to generate a stream of sub-picolitre droplets. We next discuss a straightforward droplet generation technique based on the impact of a larger droplet on a superhydrophobic mesh. Upon impact over a superhydrophobic mesh, at lower impact velocities, a single droplet is generated. At higher impact velocities, multiple droplets are ejected per impact. This technique can generate droplets over a wide range of sizes (40 – picolitre to sub-microliter). Replacing the nozzle in a conventional printer allows the printing of inks with extremely high mass loading. We discuss advances in the open-chip EWOD platform. Unlike conventional EWOD, this platform uses electrodes only on one side. This improves accessibility to the sample. The better sample accessibility enables integration of many sensing technologies with conventional platforms.

Droplet Generation at Nano & Picolitre Volumes

Microdroplet Generation using High-Frequency Electric Fields

Droplet manipulation using a high-frequency (> 10 kHz) electric field is termed Liquid dielectrophoresis (L-DEP).[57,58] Here, coplanar metal electrodes are fabricated on a glass substrate,[59,60] and the passivation layer used is either Parylene or SU8. When a high-frequency voltage is applied on the coplanar electrodes, the microliter liquid drop experiences a non-uniform electric field. The resultant dielectrophoretic force causes the droplet to elongate along the gap of the coplanar electrodes forming a cylindrical liquid column.[61] This technique has been used for various droplet functionalities such as droplet manipulation,[61] mixing of microliter droplets,[62] and droplet heating.[60] Generation of nanolitre droplets from the parent microliter droplet has also been demonstrated.[63] Multiple electrodes and a sequential actuation program are used to create droplets from bulk. However, the generated droplets are formed on the surface and are difficult to transfer to a different substrate.[63]

Nampoothiri et al. reported the use of the L-DEP technique to generate streams of micron-sized (sub-picolitre) droplets.[64] Schematic of the experimental setup is shown in Figure 1(a). The device configuration is coplanar EWOD with chromium/gold (20 nm/100 nm) electrodes on a glass surface. The gap between the electrode was fixed at 100 µm, and SU8 2005 coating (~6 µm) was used as a dielectric. The top plate was deposited with 150 nm Indium Tin Oxide (ITO). Two out-of-phase sine waves were supplied to the bottom plate for the droplet actuation, and the top plate was DC-biased. The phenomenon was recorded with a high-speed camera.

During droplet actuation using 470 V_{ac} at 50 kHz, intermittent droplet streams were observed, as seen in Figure 1(b). The droplet stream was captured on the top substrate that was placed ~3mm above the droplet. Figure 1(c) shows the image of the micron-sized droplets collected on the top substrate. The size and monodispersity of the generated and transferred droplets were controlled using an external DC bias. At higher DC voltages, a larger number of droplets were observed on the top plate, as seen in Figure 1(d). Droplet size distribution was estimated by measuring the size of 240 droplets on the top substrate. The droplet size varied from 5 μm for -250 V_{dc} bias to 7.1 μm for -1 kV_{dc} bias. The calculated drop volume varies from 65 femtolitres to 190 femtolitres. The size distribution for two DC bias voltages is shown in Figure 1(e). Relative standard deviation in the droplet size varied from 0.24 to 0.34, implying good monodispersity. The generation of the droplet stream is a complex phenomenon, which is described below.

For actuation at frequencies greater than 10 kHz, dielectrophoretic heating of the liquid takes place. This heating drives hydrodynamic flows inside the droplet. Flow within the drop for low and high actuation frequency regimes was reported by Ko et al.,[65] and P. García-Sánchez et al.[66] The fluid flow patterns observed for high-frequency actuation have been explained by Lee et al.[67] Electrothermal flows have been proven to be an effective technique for mixing in lab-on-chip applications.[68] In these studies, voltages applied were less than 150 V_{ac} at frequencies of 50–100 kHz.[66–68] Droplet heating under these actuation conditions is not significant (7-14 °C). However, significant droplet heating can occur for higher actuation voltages, as seen in Figure 2(a-c). Temperature rise increases with actuation voltage and frequency. For 460 V_{rms} at 50 kHz, a temperature increase of 38 °C was reported for DI water.[60] This kind of heating is termed as "direct heating of droplets."
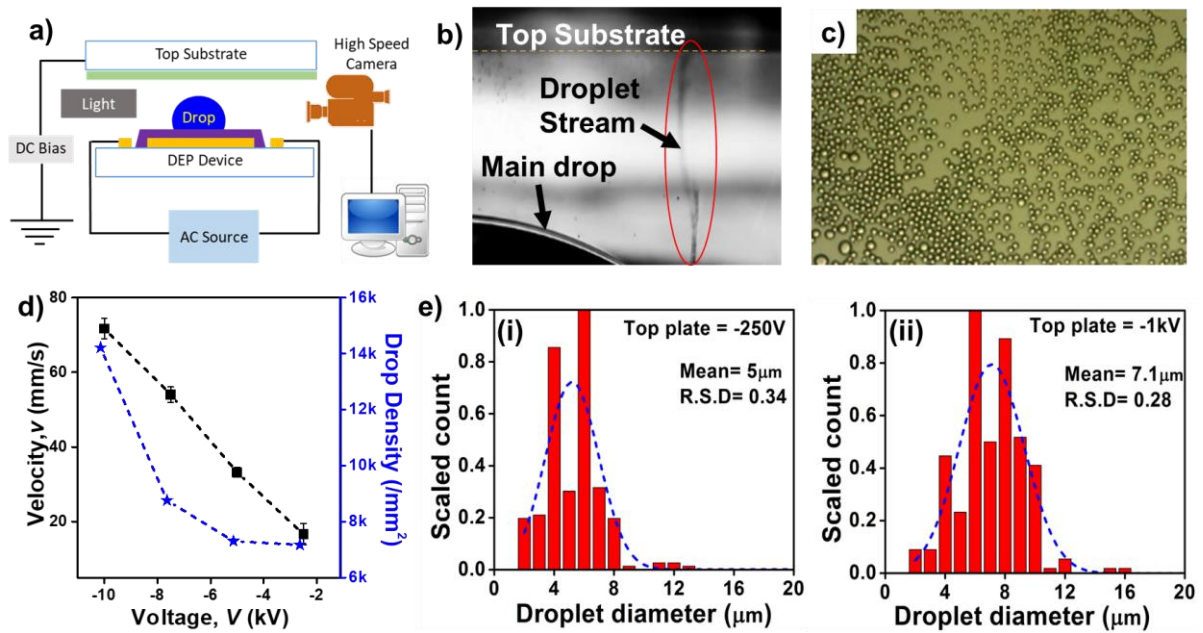
Direct Heating of Liquid Droplets

Figure 1: Sub-picolitre droplet generation in liquid dielectrophoresis. (a) Schematic of the experimental setup. An ac source is used to actuate the droplet. A dc bias on the top plate was used to control the droplet size and density. The dynamics of the jet stream was captured using a high-speed camera. (b) Image of a generated droplet stream. (c) Image of droplets captured on the top-substrate. (d) Droplet stream velocity and droplet density on the top plate as a function of the applied dc bias. (e) Size distribution for droplets at different dc bias voltages. Reprinted with permission from ref [64]. Copyright 2017 IEEE.

An equivalent circuit model of the system is shown in Figure 2(d). At low actuation frequencies, the dielectric impedance ($1/j\omega C_d$, where $\omega = 2\pi f$ is the angular frequency, C_d is the dielectric capacitance) is high and the applied voltage drops across the dielectric. The power dissipation in droplet V_{drop}^2/R_w (where V_{drop} is the voltage drop across the droplet) remains low. Beyond a critical actuation frequency, $f_{c1} = 1/2\pi R_w(0.5C_d - C_w)$, the dielectric impedance becomes smaller than the droplet impedance. The current through R_w increases and joule heating ($I_w^2 R_w$) of the droplet is observed. The displacement current through the droplet (C_w) leads to dielectric heating.[69] However, in the kHz regime, dielectric heating remains insignificant. Above a second critical frequency ($f_{c2} = 1/2\pi R_w C_w$), the current through R_w decreases as the displacement current increases. For a liquid with 0.2 mS/m conductivity, $f_{c1} = 9$ kHz and $f_{c2} = 145$ kHz was reported.[60]

The heating of the droplet actuated using coplanar electrodes is not uniform. This is primarily due to the non-uniform electric field density. The temperature variations inside the drop drive electrohydrodynamic flows.[70] Electrical properties of the liquid become non-uniform as they depend on the temperature of the liquid. In the presence of an applied field, these gradients in liquid properties give rise to a body force. Green et al.[71] have derived the time-averaged body

force by taking into consideration the variation in liquid conductivity and permittivity. It is given by

$$\langle f_e \rangle = \frac{1}{2} Re \left[\frac{\sigma \varepsilon (\alpha - \beta)}{\sigma + i\omega\varepsilon} (\nabla T \cdot E_o) E_o^* - \frac{1}{2} \varepsilon \alpha E_o^2 \nabla T \right] \tag{1}$$

Where zeroth order electric field is given by $E_0 = -\nabla\varphi_0$ with φ_0 being electric potential. $\alpha \equiv \epsilon^{-1}(\partial\epsilon/\partial T)$ represents the change in electrical permittivity (ϵ) with temperature. Additionally, T represents the temperature, and ω is the angular frequency. Similarly, the effect of temperature on conductivity (σ) is captured by $\beta \equiv \sigma^{-1}(\partial\epsilon/\partial T)$. Re denotes the real part and * represents the complex conjugate.
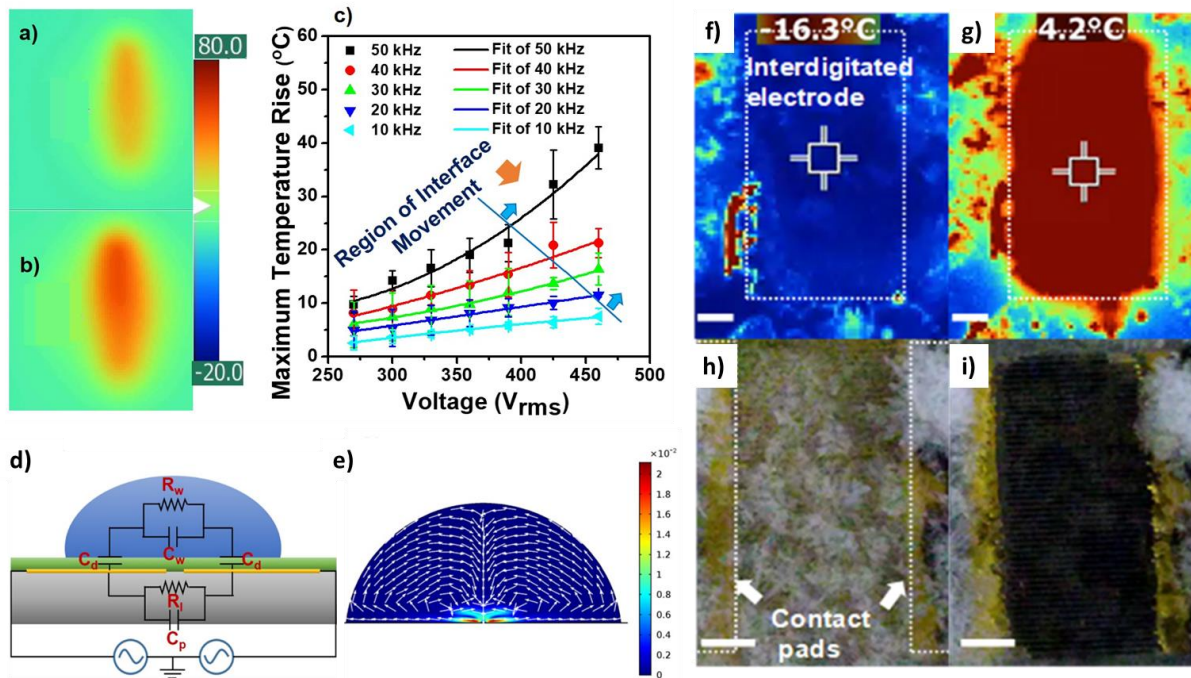

Figure 2: (a-e) Direct heating of droplets. Reprinted with permission from ref [60]. Copyright 2018 Elsevier B.V. The temperature rise of the drop as captured by an IR camera at 460 V_{rms}, 50 kHz at (a) 10 s (b) 30 s. (c) Temperature rise as a function of applied voltage at different frequencies. Data were fitted by considering the rate of heat generation by Joule heating. Temperature rise is proportional to V^2. (d) Simplified electrical circuit model for the droplet. (e) Simulation results of electrothermal flow in DI water (460 V_{rms}, 50 kHz). The velocities are reported in m/s. (f-i) Deicing application. Reprinted with permission from ref [59]. Copyright 2020 IEEE. (f-g) Images captured using an IR camera of the device at different stages of deicing (h-i) Top view images of the deicing device. Scale = 2 mm.

Equation (1) is solved with the Navier-Stokes equation and heat flow equation to obtain droplet flow and temperature[66]

$$\rho u \cdot \nabla u = -\nabla p + \mu \nabla^2 u + \langle f_e \rangle \tag{2}$$

$$\rho C_p u \cdot \nabla T = k \nabla^2 T + \langle \sigma E_0^2 \rangle \tag{3}$$

Where μ is liquid viscosity, C_p is the specific heat at constant pressure, and k is thermal conductivity. These equations were solved simultaneously in COMSOL. The simulation modeled the observed experimental trends accurately. There was also a fair quantitative match between the experiments and the simulations. The flow pattern is shown in Figure 2(e). These flow patterns are very different when compared to convective flow patterns for droplet heating using a microheater. The flow leads to a more uniform temperature distribution across the droplet.

The frequency regime and the actuation voltage required to achieve the desired temperature change vary with liquid properties. Heating at lower actuation voltages is possible for liquids with higher conductivity. This is because f_{c2} is higher for liquids with higher conductivity. Such higher conductivity allows operation at higher frequencies where almost all voltage drops across the droplet. Beyond f_{c2}, the maximum temperature saturates and does not increase with frequency.[60] In contrast to 460 V_{rms} at 50 kHz required for DI water, 0.085 mM NaCl solution can be heated to the same extent using 200Vrms at 200 kHz. The required voltage further decreased to 175 V_{rms} at 300 kHz for 0.17 mM NaCl. Further, 68 °C temperature rise (94 °C absolute temperature) was reported for 1 mM NaCl for 100 V_{rms} at 2.5 MHz.

Such a heating scheme finds use in droplet-based microfluidics applications. An interesting deicing application was demonstrated.[59] Ice was generated on dielectric coated interdigitated electrodes using a Peltier cooler. Capacitive sensing at low excitation voltages was used to detect the extent of ice formation. When 200 V_{rms} at 50 kHz was applied to the same electrodes, the temperature of the ice increased due to direct heating,[60] (Figure 2(f-g)) which led to deicing. Figure 2(h-i) shows the top view images of the device at various stages of deicing. Thus, by swapping the frequency range, the device can perform both the functionalities of ice detection (1-30 kHz) and deicing (30-50 kHz). Thus, eliminating the requirement of a separate sensor. In the absence of ice or water (dry surface), the system's energy output automatically decreases. This makes the direct heating scheme energy efficient."

Charge Induced Condensation

Heating of the droplet causes significant droplet evaporation. A vapor front is set around the heated droplet. Microdroplets with sizes of ~10-20 µm are observable on the device surface.[72] Flying droplets formed due to condensation in the air was also reported. However, nucleation in air or device surfaces cannot explain the observed streaming/jetting phenomenon. It was

hypothesized that high-electric fields in-between the L-DEP electrodes cause streams of charges to leak into the atmosphere.[72] Leakage of the charge due to dielectric breakdown at high electric fields has been reported earlier in the literature. These generated charged species from the dielectric leakage triggers localized condensation. These generated charged species provide additional nucleation sites for localized condensation.[73,74] Condensation leads to the formation of microdroplets, and these condensing microdroplets were driven by the convection current of the evaporating larger droplet. Charged species have also been shown to trigger snow formation[75] and water precipitation inside a cloud chamber.[73] The generated ions (charged species) have also been utilized to harvest water vapour from air.[74]

To verify this, Nampoothiri et. al.[72] designed a pair of devices, as shown in Figure 3(a). The vapor front was simulated by heating the primary droplet using a microheater. The high frequency ac voltage was applied on the second pair of pointed electrodes. The main droplet was heated to 63 °C using the microheater. Below a critical electric field, droplet streaming was suppressed. Above the critical electric field, intermittent droplet streaming was observed (Figure 3(b-c)). With an increasing electric field, the average time gap between two streaming events is reduced (see Figure 3(d)). The soft dielectric breakdown creates the charged species on which the liquid condensation nucleates.[75] Water vapor accumulates by molecular diffusion on the nucleating drop if the surrounding vapor pressure exceeds the saturation vapor pressure. The time difference between droplet stream ejections depends on the rate at which the nucleation sites become available. Hence, the time difference between streaming decreases as the breakdown current increases with the applied electric field. Subsequently, the voltage applied on the pointed electrode was switched. When the ac voltage on the pointed electrodes was turned off, droplet streaming disappeared. The role of spacing between the primary droplet and the pointed electrode on condensation and streaming is shown in Figure 3(e). Beyond a critical spacing, the droplet streaming is suppressed due to the decrease in relative humidity, which impedes nucleation and droplet growth. The critical spacing is larger when the primary droplet is heated to a higher temperature of 75 °C. This observation further verifies the effect of humidity.

The generated microdroplets flow with the convection current of the vapor, giving the impression of a stream. The flow can be studied by solving the Navier-Stokes equation for the gas (with vapor) given as

$$\rho_g(u \cdot \nabla)u = -\nabla P + \mu \nabla^2 u + \rho_g g \qquad (4)$$

To keep the simulation manageable, liquid flow and convective heat transfer inside the droplet is neglected. The density of the air-vapor mixture is calculated by using the ideal gas equation. Thus, $\rho_g = C_v M_v + (C_g - C_v)M$, where $C_v = P_s/RT$, $M_g = 0.029$ kg/mol, $M_v = 0.018$ kg/mol and $C_g = P_{atm}/RT$. Thermal conduction and convection for vapor phase is given by $\rho_g C_p u \cdot \nabla T = k\nabla^2 T + e_g$, where e_g accounts for sensible heat. The vapor transport through diffusion and convection is modeled as

$$u \cdot \nabla C_v - \nabla \cdot (D\nabla C_v) = 0 \qquad (5)$$

Where, D is vapor diffusivity in air. Mass flux due to the evaporation from the primary droplet is accounted for using $m_f = M_v(-D\, n \cdot \nabla C_v + v_n C_v)$. The first term represents vapor transport due to diffusion and the second term accounts for Stefan flow.[76]
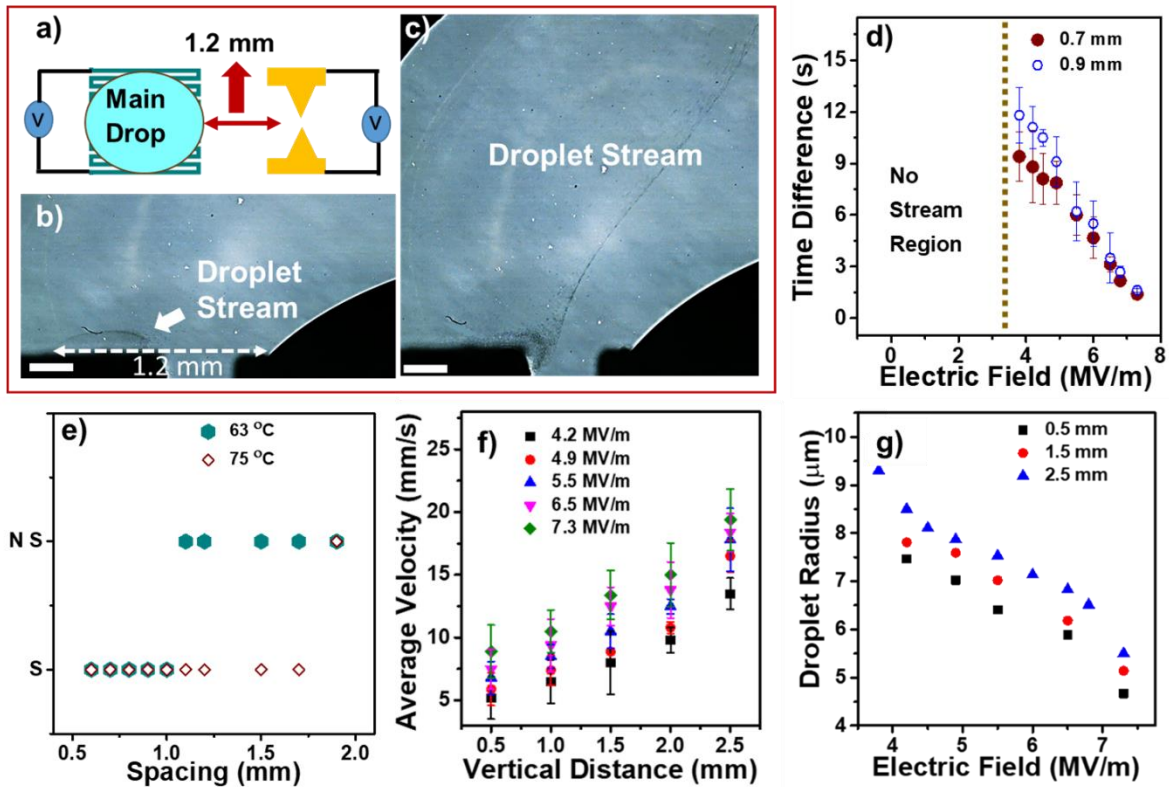

Figure 3: Charge-induced condensation. Reprinted with permission from ref [72]. Copyright 2019 Elsevier B.V. (a) Schematic of the experiment. Pointed electrodes and the micro heater are on two separate chips. (b) The stream is observed to initiate from the pointed electrodes. (c) The stream propagates along with the vapor convection currents. Scale bar = 200 μm. (d) Time difference between stream ejections plotted for different electric field magnitudes at 50 kHz for 0.7 and 0.9 mm spacing. (e) Effect of spacing on-stream formation for different droplet temperatures at 7.3 MV/m. NS: represents No Stream, and S: represents stream. (f) Measured average stream velocity at different vertical heights for varying electric fields. (g) Plot of droplet radius for different electric fields at different heights.

Simulation results showed a good match with the experimental observations. The vapor front was simulated by heating the primary droplet using a microheater. The high frequency ac voltage was applied on the second pair of pointed electrodes. The simulation indicates that the air velocity increases with the increase in vertical distance from the substrate. This behavior matches well with the measured stream velocity shown in Figure 3(f). Microdroplets in the stream are driven by the viscous drag of the flowing air-vapor mixture. A coarse estimate of the droplet size is obtained by balancing the driving force with the opposing forces of gravity and dielectrophoresis. The droplet size decrease with an increase in the ac electric field. The vapor saturation ratio (S) reduces when numerous droplets are nucleated simultaneously within a small volume. The vapor saturation ratio (S) is the ratio of actual vapor pressure to the equilibrium vapor pressure at a given temperature. Reduction in the saturation ratio limits droplet growth. A larger number of nucleation for a higher ac electric field limits the droplet's growth; hence, smaller droplets are observed at higher ac electric fields (Figure 3(g)).

Droplet Generation in 40-picolitre to Sub-microlitre Volumes

Liquid Penetration Through Superhydrophobic Sieves

Superhydrophobic flat surfaces have been explored widely for many applications related to drag reduction, self-cleaning, water harvesting, heat transfer enhancement, and anti-icing.[77–79] Similarly, the superhydrophobic mesh with sub-millimeter pores can be used for applications related to separating oil and water,[80] harvesting moisture,[81] agricultural spray,[82] repelling rain,[83,84] and capturing bubbles.[85] The mesh surface has an inherent structuring which, in combination with the nanostructured surface, leads to several interesting phenomena, such as leaky behavior, where fluid can easily pass through the holes of the sieve. Drop impacting on a flat superhydrophobic surface goes through impact, spreading, recoiling, detaching, and bouncing stages. For impact on a superhydrophobic mesh, liquid penetration and subsequent jet formation modifies these stages. The jet penetrates when the liquid pressure exceeds the anti-penetration pressure of the mesh. Several studies have quantified anti-penetration pressure for sieves of different wettability, predicting a better water penetration resistance in superhydrophobic mesh than hydrophilic or hydrophobic mesh.[86,87] Recently, Ryu et al. found a novel mechanism in drop impact which water penetrates through superhydrophobic surfaces more easily than hydrophobic surface.[88]
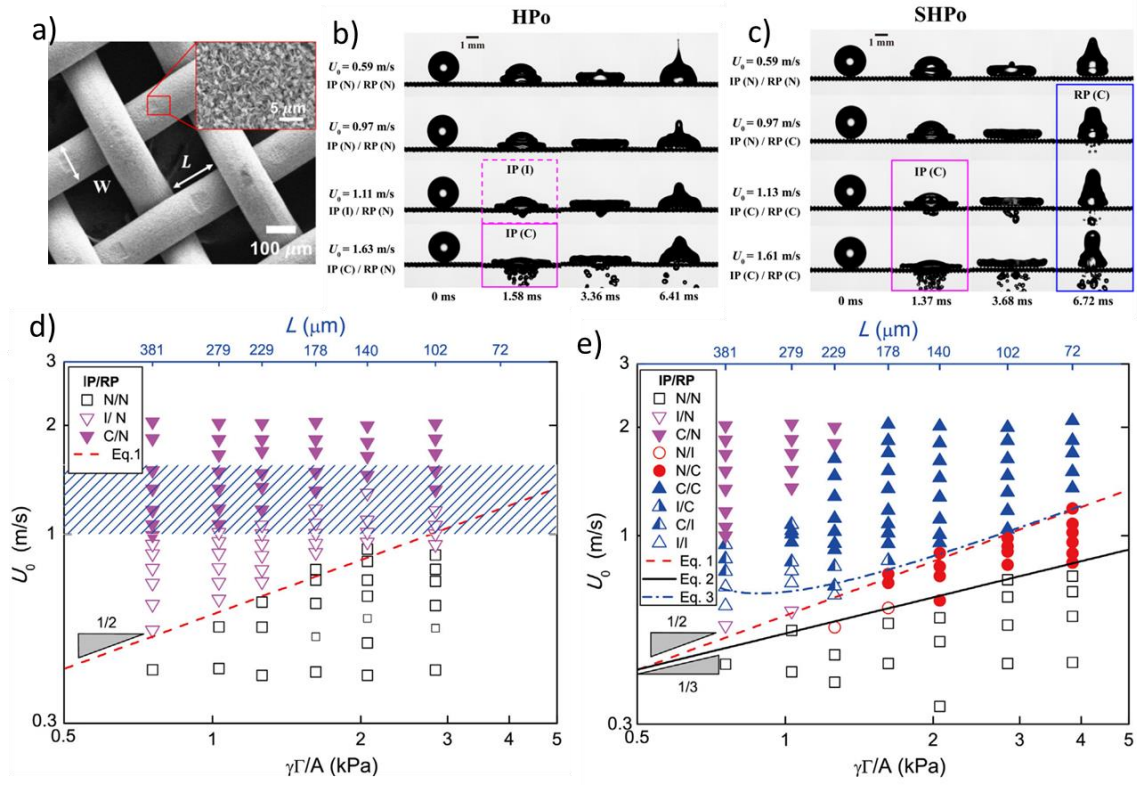
Figure 4: Penetration mechanism in hydrophobic (HPo) and superhydrophobic (SHPo) meshes. Reprinted with permission from ref [88]. Copyright 2017 American Physical Society. (a) SEM image of the copper mesh. W represents the wire diameter and L represents the pore opening. Dynamics of droplet on (b) HPo and (c) SHPo mesh with parameters W = 114.3 μm and L = 139.7 μm. Phase diagram plotted for impact velocity against anti-penetration pressure in log scale for (d) HPo and (e) SHPo meshes. N, I and C represent no penetration, incomplete penetration, and complete penetration of the droplet, respectively.

Figure 4(a) represents the copper mesh used in their experiments by Ryu et al..[88] W is the wire diameter, and L is the pore opening. For inviscid drop impact, the penetration dynamics is governed by the balance between dynamic and anti-penetration pressure. For droplet impact experiments, the droplet was generated by a syringe and allowed to fall on different meshes from different heights. The fall height of the droplet controls the velocity. The dynamics of the process was recorded using a high speed camera. The dynamic pressure can be represented in terms of momentum (M) transferred upon a surface area (A_c) over a time scale (τ), i.e., $\Delta P_{dynamic} \sim M/A_c\tau$. During impact, the momentum is given by $M \sim \rho D_o^3 U_o$, where ρ is density, D_0 is the droplet diameter and U_0 is the impact velocity. The momentum is transferred upon the area $A_c \sim D_0^2$ over a time scale $\tau \sim D_o/U_o$. This results in $\Delta P_{dynamic} \sim \rho U_0^2$. The liquid penetrates when the $\Delta P_{dynamic} > \gamma\Phi/A$, where Φ is the pore perimeter (~4L) and A is the pore area (~L^2). This is called impact penetration (IP) mode. The critical velocity for impact penetration is given by

$$U_{c,IP} \sim \left(\frac{\gamma\Gamma}{\rho A}\right)^{0.5} \tag{6}$$

Figures 4(b) and 4(c) represent the comparison of penetration behavior between hydrophobic (HPo) and superhydrophobic (SHPo) meshes. Ryu et al.[88] reported liquid penetration in superhydrophobic meshes at impact velocities lesser than $U_{c,IP}$. This mode was called recoil penetration (RP), as it was observed during the droplet's retraction. Recoil penetration was not observed in hydrophobic meshes. Figure 4(d) & (e) shows the regime plot of impact velocity with anti-penetration pressure, where the red dotted line represents Eq. (6).

When a droplet impacts the surface, the kinetic energy causes the drop to spread. The kinetic energy is converted to surface energy and dissipation due to friction. For water droplets impacting on superhydrophobic surfaces, the loss in energy due to friction is not significant and can be neglected.[89] Additionally, the restitution coefficient of a water droplet impacting on a superhydrophobic surface remains close to one, confirming negligible dissipation.[90] Thus, during recoil on the SHPo surfaces, the droplet recovers most of the kinetic energy and momentum during retraction remains the same as impact momentum. However, the relevant time scale will be Rayleigh oscillations time scale ($\tau \sim (\rho D_o^3/\gamma)^{0.5}$). Additionally, the area of penetration during recoil is comparable to jet diameter, which scales as the pancake thickness (h) at the maximum diameter (D_{max}). Since the pancake thickness varies with $h \sim \left(\gamma/\rho(U_o^2/D_o)\right)^{0.5}$,[91] the resultant penetration pressure scales as $\Delta P \sim M/A_c\tau \sim \rho^{3/2}D_o^{1/2}U_o^3\gamma^{-1/2}$. Equating it to anti-penetration pressure results in critical conditions for recoil penetration.

$$U_{c,RP} \sim \rho^{-\frac{1}{2}}D_o^{-\frac{1}{6}}\gamma^{\frac{1}{6}}\left(\frac{\gamma\Gamma}{A}\right)^{1/3} \tag{7}$$

The solid black line in Figure 4(e) represents the critical velocity of recoil penetration ($U_{c,RP}$) predicted by Eq. (7). Thus, despite higher repellence, superhydrophobic sieves are much more vulnerable to liquid penetration in droplet impact than hydrophobic sieves. The ejected jet breaks into droplets when the jet length is greater than the critical length for Rayleigh Plateau instability ($\sim \sqrt{2}\pi L$). This implies that the jet will have a higher tendency to eject droplets for decreasing pore size.

Drop on Demand using Drop Impact Printing

By controlling the impact velocity on superhydrophobic sieves, the generation of a single drop on-demand has been demonstrated by Modak et. al..[92] Here, a primary drop (mm scale) is impacted from an optimized height on the SHPo mesh. During the recoil phase, the primary drop ejects out a single microscale drop underneath the mesh. Using this regime of single drop ejection, a technique of drop impact printing[92] was developed (Figure 5(a)). Single droplet ejection happens in a regime where the impact velocity is not sufficient for impact ejection. Droplet ejection is enabled by the singular collapse of cavities formed during the drop impact. Two modes of cavity formation during droplet impact on SHPo mesh (Figure 5(b) & (c)) were reported. The impact cavity formation occurs during the initial impact phase due to capillary waves generated by inertial shock (Figure 5(b)). Interestingly, at a much lower Weber number, the liquid interface in contact with the mesh recoils back and fills the impact cavity. It further generates an inverse cavity known as the recoil cavity. Subsequent retraction of the interface results in the collapse of the recoil cavity, resulting in single droplet generation (Figure 5(c)).

The droplet ejection size depends on pore dimensions, and its range is from millimeters to micrometers scale. The largest and smallest drop size is 1 mm and 40 µm, respectively (Figure 5(d)). The recoil cavity droplet ejection occurs only for low pore-size meshes. The liquid interface cannot retract for higher pore openings because of the larger volume in the impact jet. Hence, the recoil cavity is absent. Impact cavity collapse drives single droplet ejection in meshes with larger pore openings. Thus, generated droplet size is larger than the pore size (Figure 5(d)). While for lower pore openings, the single droplet generation is governed by the cavity collapse alone, which ensures the volume is proportional to the pore opening (Figure 5(d)). Figure 5(e) represents the single droplet ejection zone for various viscous solutions prepared by mixing glycerol and water.
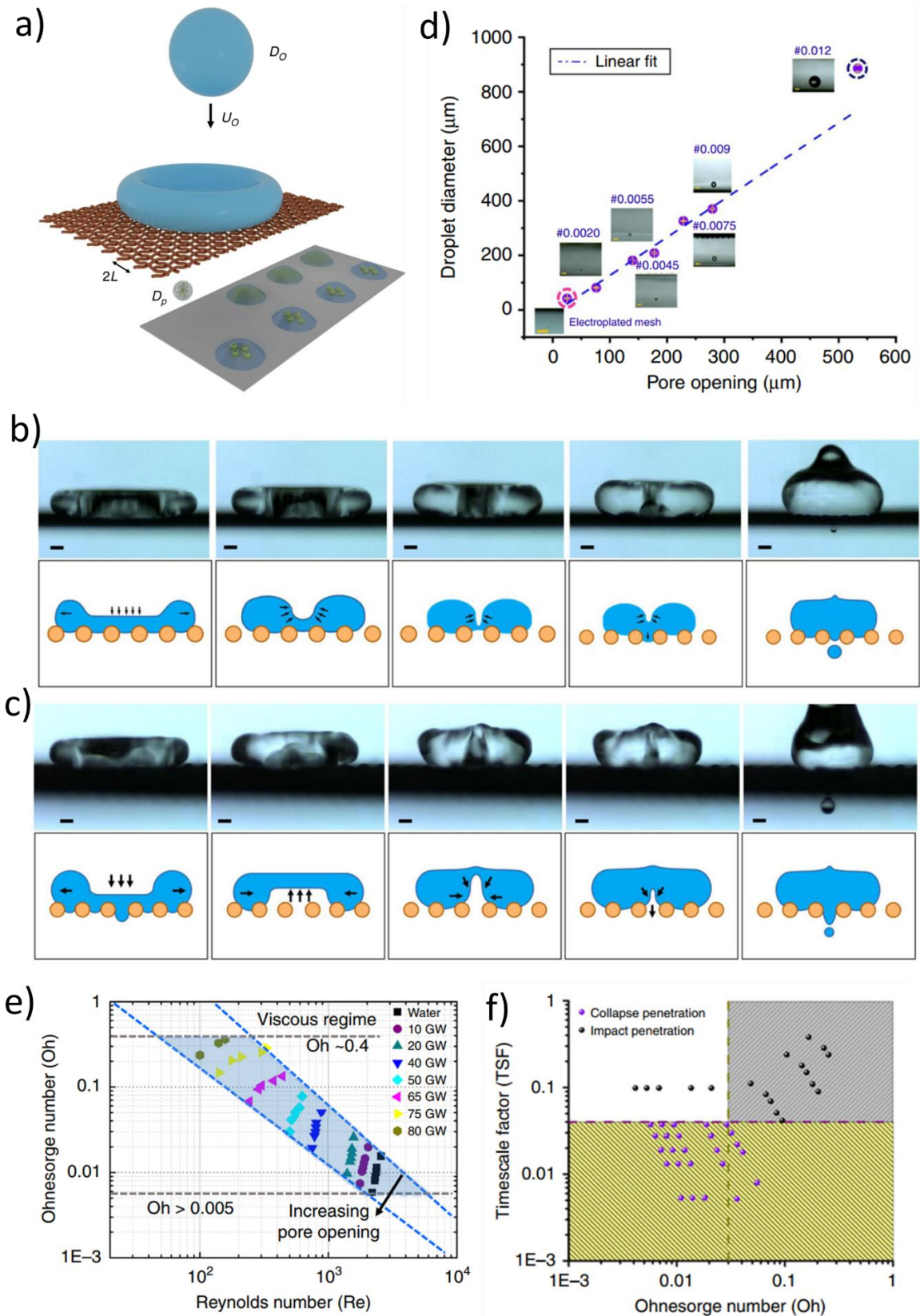
Figure 5: Single droplet generation through the mesh. Reprinted with permission from ref [92]. Copyright 2020 Springer Nature. (a) Schematic representation of drop impact setup. (b) Mechanism of impact cavity with mesh size W = 114.30 μm and L = 140 μm for 65% glycerol water mixture. Scale = 200 μm. (c) Mechanism of recoil cavity with mesh size W = 228.6 μm and L = 279 μm for a pure water droplet. Scale = 200 μm. (d) The droplet diameter varies linearly with the pore opening. However, the mesh with the highest pore opening (W = 304.8 μm and L = 533.4 μm) deviates significantly. (e) The single droplet ejection

The timescales of droplet impact and liquid penetration determine the dominant mode of ejection. In a pure inertial regime, the impact time scale is the Rayleigh time scale based on drop diameter ($\tau \sim (\rho D_o^3/\gamma)^{0.5}$), while the liquid penetration time scale is based on pore opening ($\tau \sim (\rho L^3/\gamma)^{0.5}$). Thus, the ratio between these timescales can be defined as the time scale factor (TSF) $\sim (L/D)^{3/2}$. However, in a viscous regime, the penetration time scale is given by $\tau_v \sim \mu W/\gamma$. The shift between the regime happens when the timescale for viscous flow in the pore is comparable to the inertial timescale. Thus, the timescale factor based on the critical Ohnesorge number (Oh_{cr}) can be defined as

$$
\begin{aligned}
TSF = f\left(\frac{Oh \times (W \times L^{-1})}{Oh_{cr} \times (W \times L^{-1})_{cr}}\right) &\times (L/D)^{3/2}\\
f(x) = 1, \text{ for } Oh &< Oh_{cr}\\
f(x) = x, \text{ for } Oh &\geq Oh_{cr}
\end{aligned}
\tag{8}
$$

Figure 5(f) represents the TSF for different Oh. The critical value of TSF, separating two regimes, is found to be 0.04.

Drop impact printing is a nozzle-less technique with several advantages over other techniques. The conventional printing techniques reported so far used optimized inks[28,29] and are limited by particle size[93] and concentrations.[25] This is due to narrow nozzle sizes, which tends to clog with larger particle size or concentrations. Clogging occurs due to the rapid evaporation of solvent[11,29] at the liquid nozzle interface, leading to particle settling. Different strategies, like covering the ink interface with an oil layer,[94] chemically modifying the ink,[25,28] etc., are adopted, but this all comes at a cost. Sometimes the setup becomes expensive,[24] or the technique becomes quite complex.[95] The drop impact technique has a very short contact time between the drop and the surface, so evaporation-driven settling of particles can be avoided. Due to its inherent benefit, the mesh technique was used for printing high-concentration and large particle-size inks. The maximum particle concentration reported is 71% (w/w), and the particle size is ~ 20 µm (Figure 6(a)). The reported particle concentration is three times higher than conventional printers. Additionally, the printed feature size is found to be independent of mass loading (Figure 6(b)).
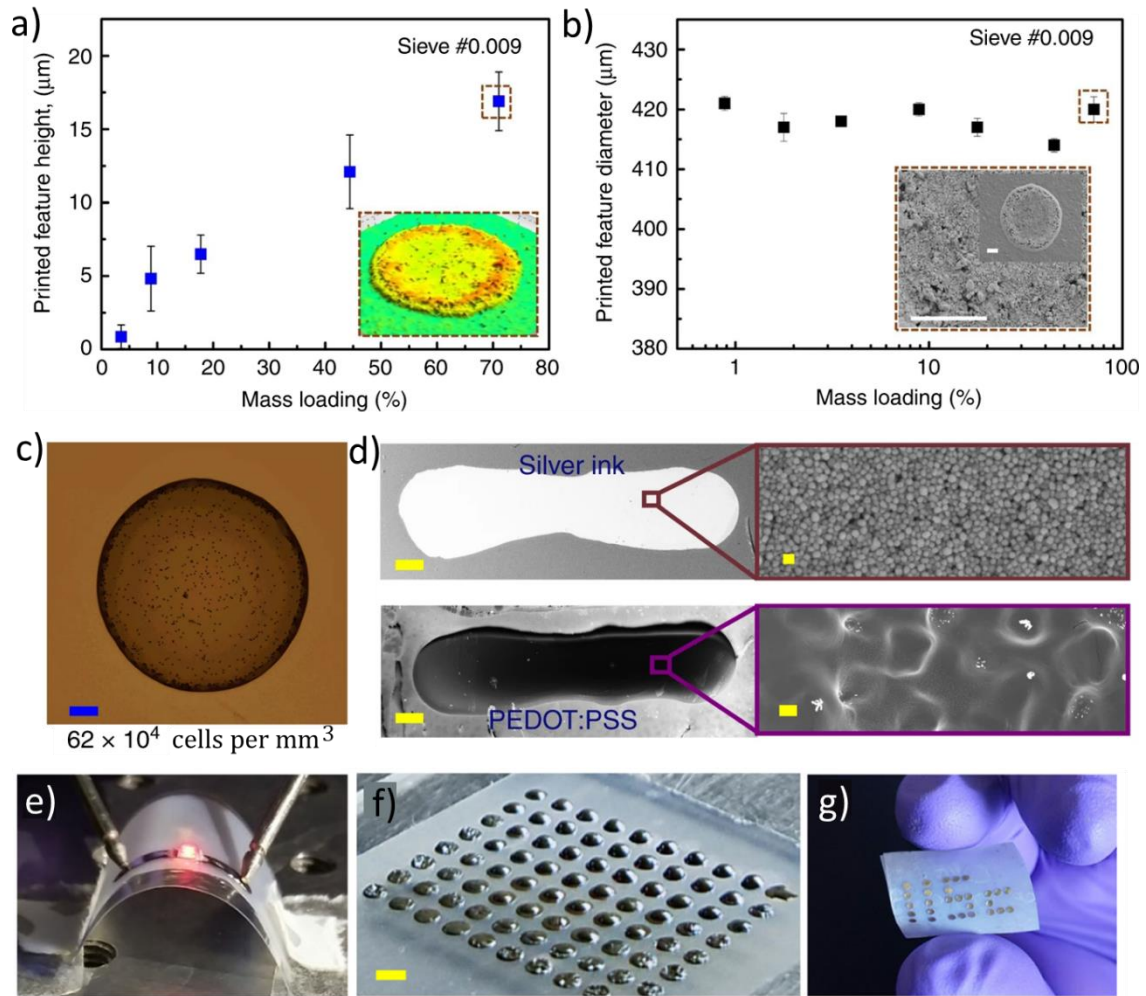
Figure 6: Applications of drop impact printing. Reprinted with permission from ref [92]. Copyright 2020 Springer Nature. (a) Height of the printed feature with mass loading variation. The inset shows the printed droplet with 71% mass loading. (b) The printed feature diameter does not vary significantly with mass loading. The inset shows the SEM image of the deposited particles. (c) RBC-laden PBS droplet produced from drop impact printing. Scale = 50 μm. (d) Continuous line printing of silver (4% v/v) and PEDOT:PSS. Scale = 200 μm. (e) Continuity check for the printed silver line. LED glows when voltage is applied across the line. (f) Droplet printing in a large area. Scale = 1 mm. (g) Flexible surface printing.

Similarly, drop impact printing is also suitable for many different applications such as cell printing (Figure 6(c)), printing circuits (Figure 6(d) and (e)), droplet array, and printing on flexible surfaces (Figure 6(f) and (g)). A summary of the comparison between different techniques is presented in Table 1. The drop impact printing performs approximately same as other commercial techniques in terms of resolution without any nozzle clogging issue. Additionally, the range of ink viscosity remains same as other drop on demand techniques. The ability to handle the high mass loading inks (~ 71 %) and particle size (~ 20 μm) without any clogging issue is the biggest advantage of drop impact printing. The generation of microscale droplets on-demand has potential in different applications like droplet arrays for gene expressions,[96] compartmental cell culture,[97] printing of electronic circuits,[98] 3D manufacturing,[99] drug fabrication industries[100] etc. Drop impact printing can be used for these

advanced applications. Apart from this, the technique opens up an avenue for high mass-loading printing. For example, printing conductive electronic lines with a single pass on porous substrates is now possible using this technique. High-mass loading printing reduces processing time and enables 3D printing.

Table 1: Comparison of different techniques with drop impact printing technique. The comparison present range of liquid properties, mechanism of drop generation, advantages, and disadvantages.

	Drop on demand (DoD) (Piezo based) Printing	Continuous (Piezo based) Printing	Electrohydrodynamic Printing	Acoustophoretic Printing	Drop Impact Printing, (DIP)
Resolution, μm	25	20	10	37,130	42
Ink Viscosity, mPas	3 – 35	2- 10	~1000	0.5 - 25,000	<33
Ink Surface tension, mNm^{-1}	44 - 54	20 – 35	NA	~25 – 624	32-72
Position accuracy, μm	66	Low	10	60 - 110	10
Mass loading (%)	<20	~10	~30	NA	71
Max particle size, μm	<0.1	<1	<1.5	10	20
Nozzle diameter, μm	5	60	5-1000	13 - 140	25 – 533
Droplet detachment mechanism	Pressure waves	Pressure waves	Electrohydrodynamic instability	Acoustic focusing	Cavity collapse induced pressure wave
Energy source	Piezo/thermal driven	Piezo/thermal driven	Voltage driven (Voltage<10kV)	Acoustic radiation pressure	Gravity driven
Working distance, mm	1	5-20	4.5 – 5.5	3.15 – 5.15	1-5
Ink palette	Mostly all inks	Conductive charged inks	Conductive inks, viscous inks	Mostly all inks, high viscous inks	Mostly all inks
Drop volume	1 pL – 8 pL	4 pL -1.76 nL	2 pL - 135 pL	1.15 nL - 2.145 μL	38 pL – 463 nL

Drop height /drop width (single drop)	~0.004	~0.0014	~0.01	NA	~0.3
Drop on Demand	Yes	No	No	Yes	Yes
Cost (printhead), $	100-1000	100-1000	Low cost	NA	9.4
Nozzle Clogging	Yes	Yes	Can be minimized up to some extent	Less clogging	No

Multi-Droplet Ejection using High-Velocity Impact on Meshes

It is important for many industrial and agricultural applications to generate and eject a large number of small droplets. For this high-velocity impact of droplets on superhydrophobic sieves can be used.[101] However, for high-velocity impact, several interesting phenomena are observed.[102] These phenomena need to be accounted for when developing such multi-drop dispensing applications. Figure 7(a) shows the behavior of the droplet impacting the same mesh at two different Weber numbers. At higher Weber numbers, it is observed that there is an early rebound of the droplet. The droplet leaves the surface in its extended state. This mode of recoil is also known as pancake bouncing.

Once the ejected jet breaks into droplets and dissociates from the main droplets, the jet interface recoils back through the mesh pore. This recoiling interface provides the required kinetic energy for the droplet to leave the surface. Pancake bouncing reduces the contact time significantly, as seen in Figure 7(a). As seen in Figure 7(b), the droplet contact time significantly decreases once the ejected volume is larger than a critical volume. Mesh #0.009 with a smaller breakthrough pressure ($\gamma\Phi/A$) transitions to the pancake bouncing much earlier than mesh #0.0045.

Compared to conventional "pancake bouncing" on flat surfaces,[103] on meshes, pancake bouncing is observed at a higher Weber number. This is because the stored energy in the penetrating interface is lost with the ejected jet. To understand the effect of pore opening on the critical Weber number for "pancake bouncing," we have to consider the adhesion force that the recoiling interface has to overcome. The liquid adhesion force scales as $\sim 4L\gamma \times n \times cos\theta_r$, where θ_r is the receding contact angle, and n is the number of holes $\sim D_0^2/(L + W)^2$.

Thus, for lower pore opening meshes while keeping the surface fraction similar, the pancake bouncing happens at a higher Weber number due to a higher adhesion force $F_{adh} \propto 1/L$. This is observed in Figure 7(b). Here, the surface fraction is the projected area of solid surface in meshes (Surface fraction = area of solid/total area of mesh).
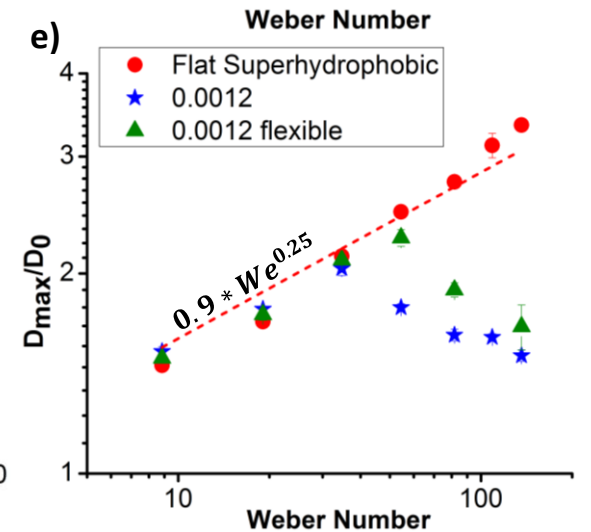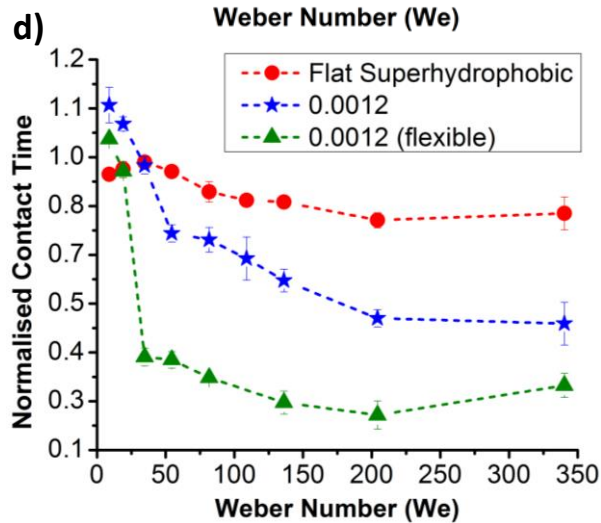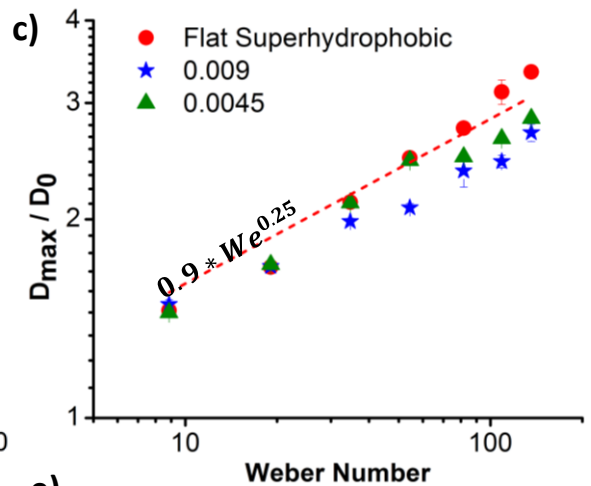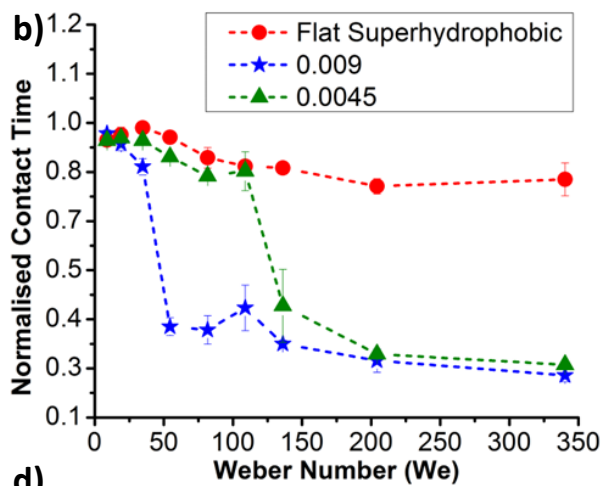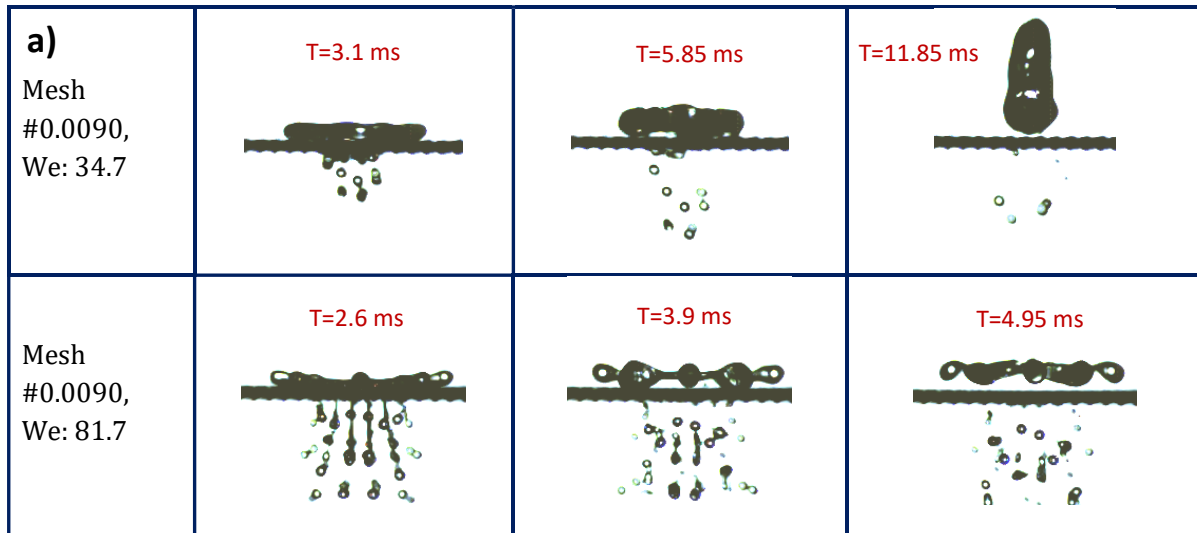
Figure 7: Effect of geometry on Droplet dynamics. Reprinted with permission from ref [102]. Copyright 2018 The Royal Society of Chemistry. (a) Sequential images representing dynamics of droplet impact on different meshes. (b) Effect of mesh parameters on normalized contact time of the droplet (Normalized by Rayleigh oscillation time). The solid fraction of the mesh is constant ($\phi = 0.7$). (c) Effect of mesh parameters on the maximum spreading of the droplet. The solid fraction of the mesh is constant ($\phi = 0.7$). (d) Effect of the flexibility of mesh on normalized contact time. The mesh used here has W = 30.48 μm, L = 224 μm, and $\phi = 0.23$. (e) Effect of the flexibility of mesh on maximum spread diameter. The mesh used here has W = 30.48 μm, L = 224 μm, and $\phi = 0.23$.

The maximum diameter of the drop is affected by jet ejection through the pores. As seen in Figure 7(c) the maximum diameter is less than on solid surfaces. The decrease in maximum diameter is ascribed to the loss of liquid volume in the form of the jet through pores. The maximum spread diameter of the impacting droplets on solid surfaces is known to follow the Weber number power law, i.e., $D_{max}/D_o \sim We^{0.25}$ (Figure 7(c)). The critical Weber number beyond which the maximum diameter deviates from the flat surface depends on the breakthrough pressure. An increase in Weber number also increases the volume loss through pores; thus, maximum spread significantly deviates from the standard power law at a higher Weber number (Figure 7(c)). Further, higher leakage can be seen if the solid fraction (ϕ) of the mesh is low, resulting in significant deviation compared to higher solid fraction meshes (Figure 7(c)).

Reduction in primary drop volume due to jet ejection leads to a reduction in its volume. This reduction in volume is reflected in a slight decrease of the droplet contact time over a rigid mesh, as seen in Figure 7(d). This is because contact time scales as the Rayleigh time ($\sim (\rho D^3/\gamma)^{0.5}$). This gradual decrease in the contact time due to volume loss is different from the step change in the contact time as seen in the case of pancake bouncing Figure 7(b). Figure 7(d) shows the effect of the flexibility of mesh on the maximum spread. Due to flexibility, the volume loss through pores is less than the rigid surface, implying a higher maximum spread than the rigid mesh. Additionally, in flexible surfaces, early pancake formation can be seen (Figure 7(e)). This is due to stored elastic energy in the flexible mesh due to droplet impact, which transfers back to the droplet during recoil.

Droplet Generation and Manipulation at Microliter Scale

Open Chip EWOD

Electrowetting-On-Dielectric (EWOD) is one of the most promising methods of droplet manipulation due to its ability to work with extremely small volumes. Further, it is portable,

programmable, reconfigurable, and low-cost. In EWOD, creation, actuation, merging, mixing, and splitting are the fundamental droplet-based operations that enable a wide array of assays. Droplets are, however, sandwiched between the two substrates in EWOD. Hence, the fluid samples can be accessed at the device edges only. It has been demonstrated that EWOD actuation is possible with a single substrate only.[104] This open-chip EWOD improves droplet accessibility and enables easy integration with external sensors and actuators. However, mixing, splitting, merging, and other operations have remained challenging. We review advances that have addressed these issues on an open chip platform.

Compound Droplets
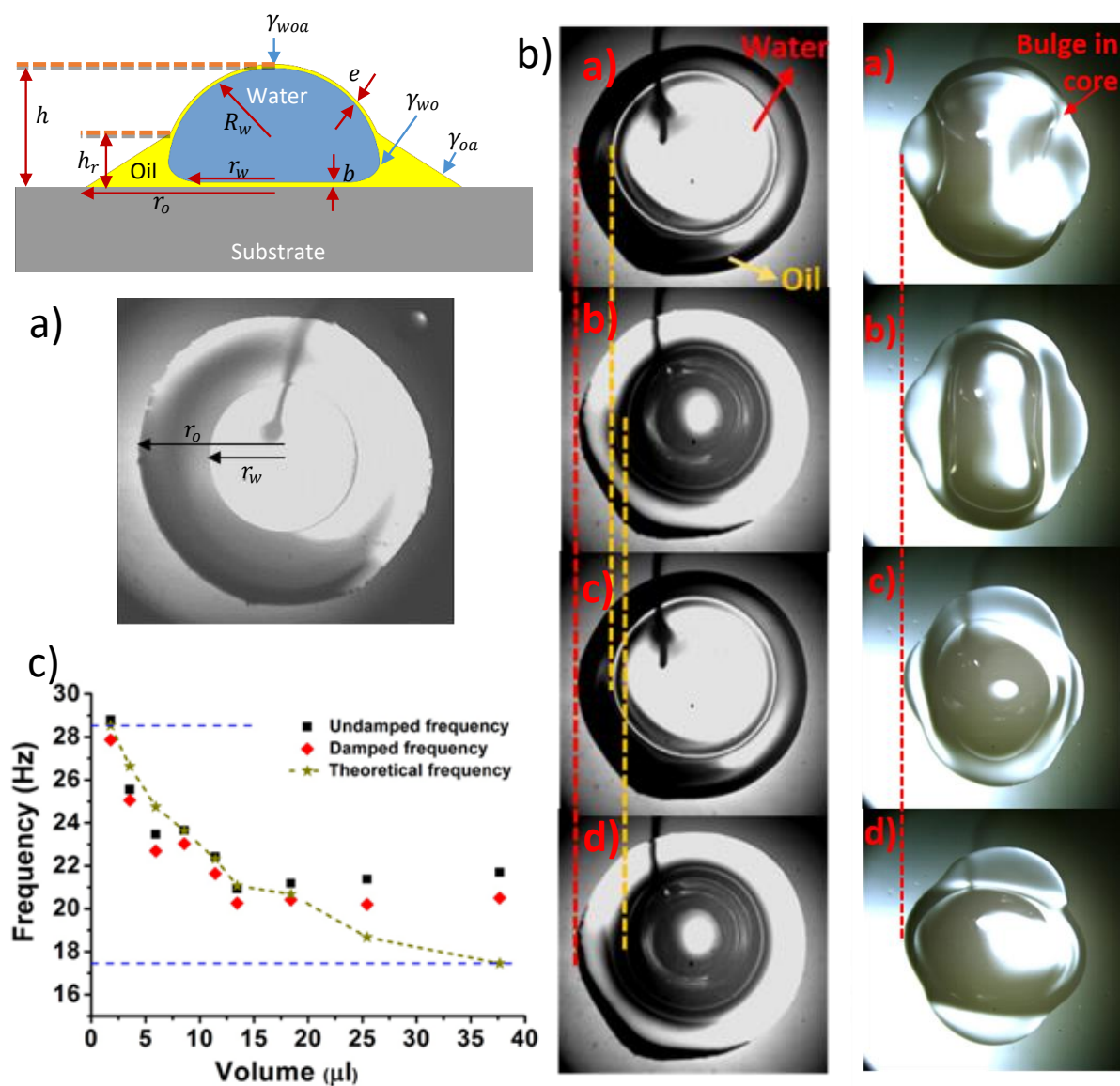

Figure 8: Compound droplet actuation. Reprinted with permission from ref [46]. Copyright 2017 American Chemical Society. *(a) Interfacial energies in compound droplet configuration and bottom view of the interface. (b) Sessile compound drop*

undergoing axisymmetric (left) and non-axisymmetric oscillations (right) using ac electrowetting as seen from the bottom view. The core droplet boundaries are bounded by the constraint of the oil shell. They form an irregular ripple or burble. Where the red dotted line represents the outer oil shell, and the yellow dotted line represents the inner liquid shell. (c) The resonant frequency of the compound droplets for different shell volumes. A semi-empirical approach gives a reasonable match to the experimental results.

The open-chip EWOD suffers from contamination and evaporation problems due to the absence of the top coverslip. One approach to resolve this is to cover the sample droplet (core) with an oil shell, as shown in Figure 8(a). This configuration is also called a compound droplet.[105] Due to favorable wetting conditions ($\gamma_{aw} > \gamma_{ao} + \gamma_{ow}$) the oil forms a shell around the droplet. Disjoining pressure stabilizes the thin film ($e \sim 62$ nm) covering at the top. The oil also forms a thin film ($b \sim 21$ nm) in between the drop and the substrate as $\gamma_{ws} > \gamma_{wo} + \gamma_{os}$. These oil film thicknesses were determined by balancing the disjoining pressures and interfacial pressure at water-oil and oil-air interfaces.[46] By approximating that the cloaking oil film follows the same curvature as the core droplet at the top, its equilibrium thickness (e) was determined as $e^3 = \left(\frac{A_{H2}R_w}{12\pi\gamma_{oa}}\right)$ where R_w is the radius of the compound drop and A_{H1}, A_{H2} are the Hamaker constants. Similarly, the bottom film thickness was estimated as $b^3 = \left(\frac{A_{H1}R_w}{6\pi(2\gamma_{ow}+\rho_w ghR_w)}\right)$ which came out to be ~ 21 nm, where h is the height of the compound droplet, and ρ_w is the density of the water core. While it remains difficult to directly measure the film thickness at the top, the thickness of the film trapped between the drop and the substrate have been measured using interferometric techniques.[106] The oil film eliminates contact angle hysteresis and allows core motion at lower actuation forces. However, this oil film is unstable at higher actuation voltages (> 98 V) when the electrostatic forces become larger than the stabilizing surface forces and van der Waals interactions.

Rayleigh gave the resonant frequency for freely oscillating spherical non-viscous liquid droplets as, $\omega_k^2 = \gamma k(k-1)(k+2)/\rho R^3$, where $k = 2,3,...$ corresponds to the mode number for droplet oscillation modes. It is equivalent to the order of spherical harmonic function which is used to define the droplet mode shape.[107–109] Modes of oscillations are represented in Figure 8(b). This expression was modified by Lamb to account for the effect of external fluid.[110] To account for multiple modes, a semi-empirical model was proposed by Noblin et al..[111] This model also accounted for pinned or mobile contact lines. These approximate models have provided a good match with various experimental results. Recently, a more detailed model for mode shapes of sessile droplets has been proposed by Bostwick and Steen.[112,113]

The dynamics of the core droplet are affected by the droplet shell.[46] The experiments were performed on 10 μl water droplets with variable silicone oil volumes. An ITO-coated glass was used as the bottom electrode, and another electrode was inserted by probing the droplet from the top side. The droplets were actuated by applying a voltage between two electrodes. The high-speed camera was used to capture the dynamics of the droplet. Droplet response to electrostatic actuation was studied by applying sinusoidal actuation. At low actuation voltages (53 V_{rms}), the contact line remains symmetrical as the droplet expands and contracts. Like a bare droplet, the compound droplet also shows different resonance modes. However, the resonant frequency strongly depends on the shell volume, as seen in Figure 8(c). Only a thin oil shell covers the core droplet for smaller shell volumes. A semi-empirical relation gives the resonance frequency,[111] accounting for the effective surface tension of the compound droplet ($\gamma_{owa} = \gamma_{ow} + \gamma_{oa} + A_H/4\pi e^2$, where A_H is Hamaker constant, and e is the film thickness). The oil-water interface energy defines the droplet response in the opposite regime of very high shell volumes. The semi-empirical model can be extended to give a resonance frequency [111]

$$\Omega_0^2 = \frac{\gamma_{ow}q^3 \tanh(qh)}{\rho_w + \rho_o \tanh(qh)} \tag{9}$$

where $q = 2\pi/\lambda$, with λ being the wavelength of the interface wave. A semi-empirical approach was used to interpolate between the two limits for intermediate shell volumes.

$$\Omega_0^2 \propto \frac{\gamma_{eff}q^3 \tanh(qh)}{\rho_{eff}} \tag{10}$$

where effective surface tension is given by $\gamma_{eff} = \gamma_{ow} + (1 - h_r/h)\gamma_{oa}$, with heights h_r and h defined in Figure 8(i). effective density ρ_{eff} is defined as $\rho_w + (h_r/h)\rho_o\tanh(qh)$. The match between the theory and the experimental results is shown in Figure 8 (iii).
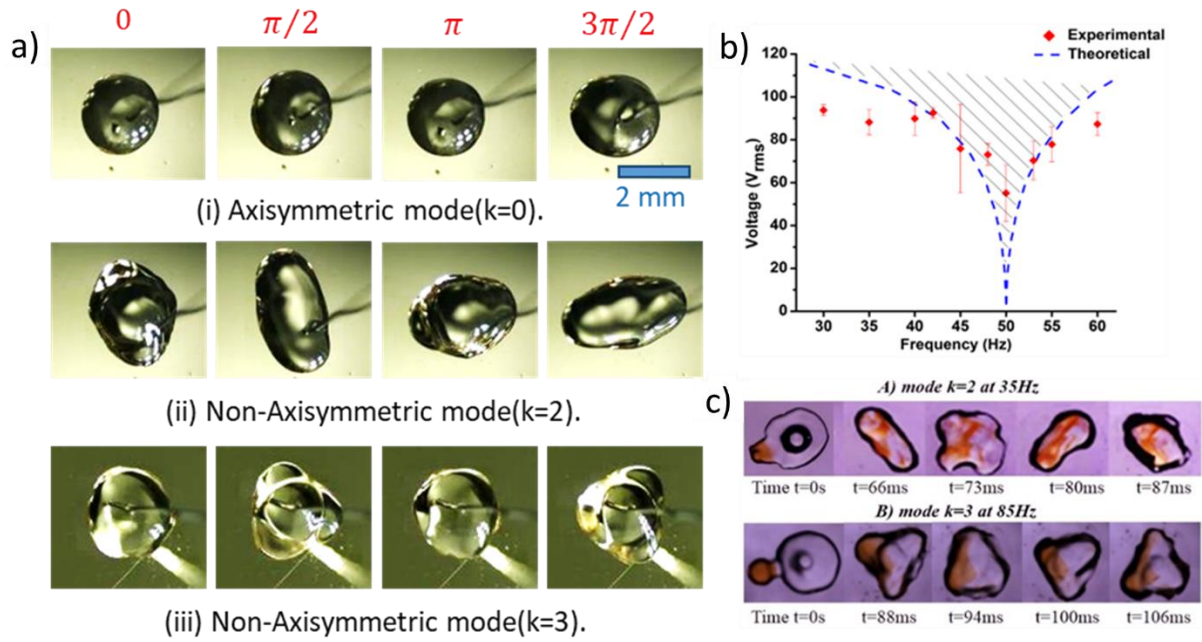
Parametric Oscillations for Mixing

Figure 9: Parametric oscillations. Reprinted with permission from ref [51]. Copyright 2016 Elsevier B.V. (a) Oscillation patterns (top view) of an 8μl droplet at different actuation voltages and frequencies k corresponds to the mode number for droplet oscillation modes. It is equivalent to the order of spherical harmonic function which is used to define the droplet mode shape. (i) mode $k = 0$ at 35 Hz, 74 V_{rms}; (ii) mode $k = 2$ at 35 Hz, 117 V_{rms}; (iii) mode $k = 3$ at 100 Hz, 117 V_{rms}. (b) Comparison of theoretical and experimental actuation (voltage and frequency) region for obtaining non-asymmetric mode $k = 2$. (c) Images of two droplets, one of DI water (8μl) and a diluted orange food colour droplet (2μl) mixed using non-asymmetric oscillations with 115 V_{rms} and frequencies (a) 35 Hz (mode $k = 2$) and (d) 85 Hz (mode $k = 3$).

On actuation at higher voltages (88 V_{rms}), the compound droplet loses its circular symmetry, and non-axisymmetric modes become visible. Non-axisymmetric drop oscillation was observed by Sen et al. and Miraghaie et al. [114,115] for certain voltages and frequencies of EWOD actuation. Ko et al.[116] observed sub-harmonic behavior during bubble oscillations. The first study of non-axisymmetric droplet oscillations using EWOD was reported for the sandwich droplet scenario.[117] Bansal et al.[51] studied non-axisymmetric oscillation of droplets in an open-chip configuration.

In non-axisymmetric oscillations, the droplet's contact line loses its circular shape during spreading and expands to asymmetrical patterns, as shown in Figure 9(a). The number of lobes represents different mode shapes. Non-axisymmetric droplet modes appear due to the parametric coupling and grow at the expense of the axisymmetric modes.[46,51,108,109] The parametric coupling arises from radius variation, which leads to $\Omega^2 = \Omega_0^2(1 - 3\Delta R/R_0)$. Non-axisymmetric modes are degenerate modes that can be controlled by varying the actuation parameters of voltage and actuation frequency.[46,51] The non-axisymmetric modes are sectoral modes, which are parametrically driven through variation of droplet radius during axisymmetric oscillations. The non-axisymmetric modes are referred to be degenerate as they

are observed at the same frequency as the axisymmetric mode. Actuation parameter regime where the parametric coupling occurs to transfer energy from axisymmetric to non-axisymmetric modes is shown in Figure 9(b). This regime where non-axisymmetric regimes are observed is expressed as $\Omega(1 - 0.5h)^{0.5} < \omega < \Omega(1 + 0.5h)^{0.5}$, where h is the amplitude of parametric variation. These non-axisymmetric oscillations were used to enhance the mixing (i.e., reduce mixing time) of reagents on an open chip, as shown in Figure 9(c) for two water droplets. Compared to mixing by pure diffusion, non-axisymmetric modes lead to 37 times faster mixing of droplets.[51]

Non-coalescence of Droplets

The merging of droplets is an essential operation in droplet-based microfluidics. The viscous effects of the thin oil film separating the two droplets hinder merging. Various external forces have been used to destabilize the oil film and enhance the merging of immersed droplets.[51,68,114] Electrowetting forces were investigated by Bansal et al..[48] Different regimes of enhanced coalescence, and prolonged non-coalescence were reported. In the case of prolonged non-coalescence, the two droplets keep oscillating without merging for durations more than 30 minutes, as seen in Figure 10(a).

The transition from coalescing to the non-coalescing regime depends on the mode amplitude of the oscillation. At intermediate actuation amplitude and low frequencies, periodic modulation stabilizes the entrapped oil film between the cores. During the retraction of the droplet interface, the outer oil flows back into the gap between the droplets. Such a phenomenon is termed as capillary pushing. The capillary pushing of the cores with a time period faster than the drainage time of the oil bridge caused the oil to flow back into the bridge during the droplet retraction. This prevented continuous drainage of the oil bridge. The oil bridge width remained constant. This explains the non-coalescence of the core droplets for a certain range of frequencies and voltages.[48] At lower actuation voltages or higher actuation frequencies, the amplitude of the droplet motion is insufficient to stabilize the oil bridge, and coalescence was observed. At higher actuation voltages, the interface motion was irregular and violent. The oil film was destabilized, and droplet merging was observed (Figure 10(b) and (c)).
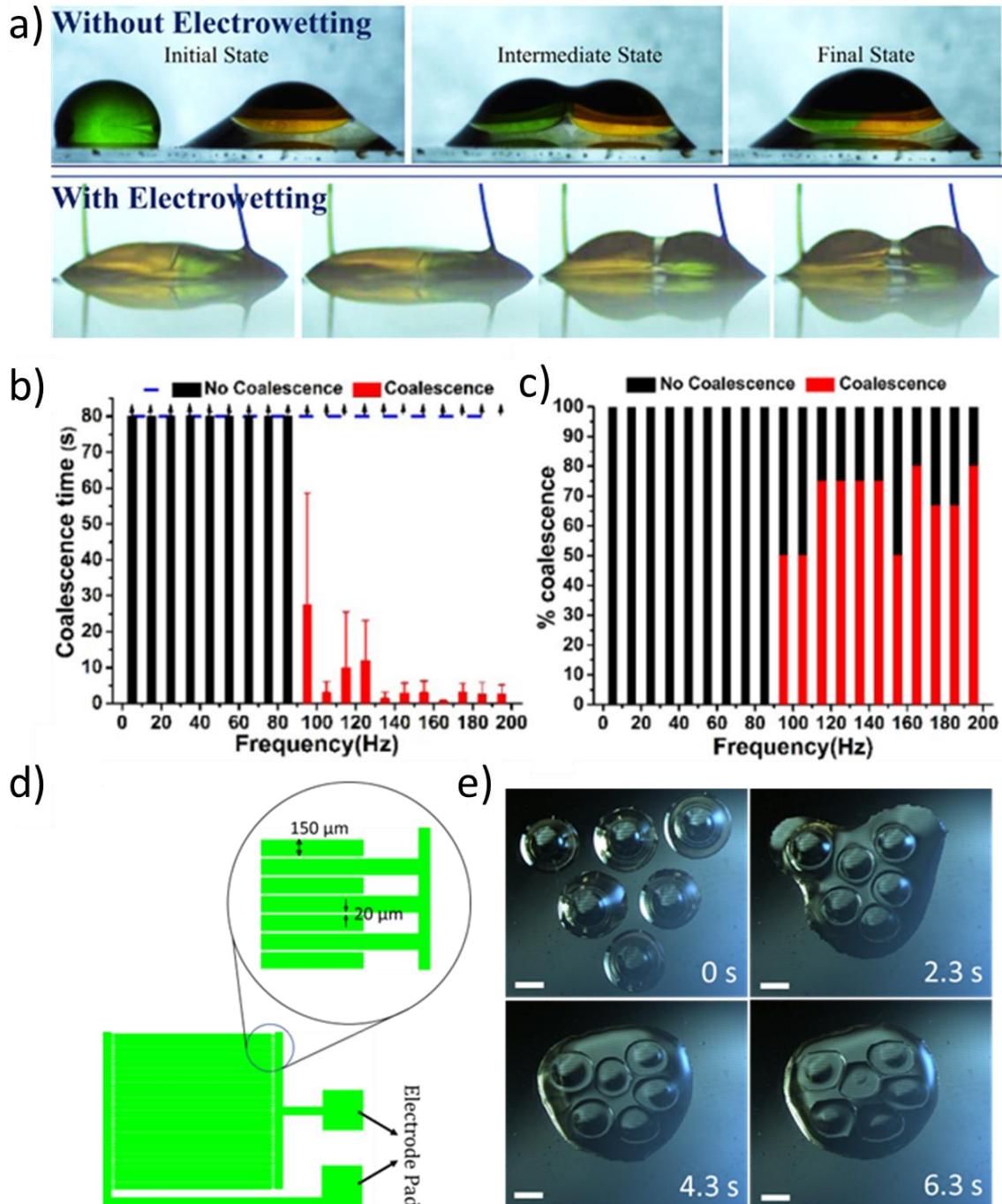
Figure 10: Droplet Non-coalescence on EWOD. (a) Experimental images for merging of compound droplets where images (top) depict coalescence and (bottom) depict non-coalescence. EWOD actuation conditions for the images in the bottom: 106 V_{rms} at 145 Hz. (b) Coalescence time at different actuation frequencies and 106 V_{rms}. The black arrows depict that the coalescence time was larger than the experiment time limit (> 80 s). (c) The number of times (in percentage) non-coalescence was obtained by repeating the experiment at the same frequency and voltage. Reprinted with permission from ref [48]. Copyright 2018 Elsevier B.V. (d) Interdigitated electrode (IDT) pattern for planar EWOD device. (e) Six droplets of 5 µl showed non-coalescence on a planar EWOD device at 15 Hz, and 200 V. Reprinted with permission from ref [118]. Copyright 2022 Springer Nature.

As shown in Figures 10 (d) & (e), the coplanar interdigitated electrode design can be employed to accommodate more droplets.[118] Prolonged non-coalescence was observed for up to six droplets. The effect of two dissimilar volumes on the fate of coalescence was studied. In this

study, three different volumes of the core droplet (5, 10, and 15 µL) were investigated. A critical amplitude of oscillation that is required for the non-coalescence of droplets as the function of applied frequency was obtained. Non-coalescence of two dissimilar droplets was observed when the largest droplet showed oscillations above a critical amplitude. The non-coalescence regime was obtained for the applied voltage and frequency. Such pro-longed non-coalescence can be used to maintain stable non-merging of droplets on the substrate and is required for various applications like compound lenses.

Single Sided Splitting

Droplet splitting is one of the important unit processes in digital microfluidics. Droplet splitting has been demonstrated in the closed-chip format in electrowetting. In this technique, the droplet is squeezed using a cover plate. In a study by Cho et al.[49] for closed-chip splitting, a smaller gap between the bottom substrate and cover plate has been suggested to assist the splitting of droplets. In the recent work by Sagar et al.,[119] an energy-based model has been developed to explain the challenge in open-chip droplet splitting. To demonstrate this, a pair of electrodes is fabricated with varying inter-electrode gaps (Figure 11 A). The droplet is placed at the center such the droplet's contact line touches both electrodes. Surface evolver simulations were carried out for various device geometries by varying the pad contact angle from 50° to 110°. The simulation assumed that for the droplet to spontaneously split in an open-chip configuration, the quasistatic surface energy should continuously decrease with a decrease in the neck width. The simulation proved that the critical pad contact angle required for splitting is quite lower than what can be achieved using electrowetting, as seen in Figure 11 (b). It shows that the threshold pad contact angle required to split the droplets lies below 60°. However, the contact angle achievable in electrowetting is around 80° due to contact angle saturation.

Open-chip splitting was pursued using compound droplets. The compound droplet was placed in the inter-electrode gap. The electrodes were made on an ITO-coated glass substrate. A DC pulse was applied across the pad to split the droplet. Droplet size, inter-electrode gap, and applied voltage were varied to obtain the regime plot for the symmetrical and asymmetrical splitting of compound droplets, as seen in Figure 11(c). The smaller normalized gap and electrowetting number favour asymmetrical splitting. The asymmetrical splitting at lower voltages is attributed to the low actuation force available for splitting. At low actuation forces,

the flow velocities are small, and inherent system asymmetries can make the configuration asymmetric. As the gap and electrowetting number are increased, we observe symmetrical splitting. Contact line hysteresis is reduced due to the oil film between the substrate and the droplet. This enables easy interface motion. Further, the core droplets' neck formed in the electrode gap does not contact the substrate. This is because the electric field does not destabilize the oil film. In contrast to a sessile neck, the cylindrical neck breaks easily by the Rayleigh-Plateau instability. At the boundary of these regimes, we observe both symmetrical and asymmetrical splitting. Blue triangles show these data points in Figure 11(c). The outcome is stochastic, and the mixed outcome results from the random heterogeneities in the system.
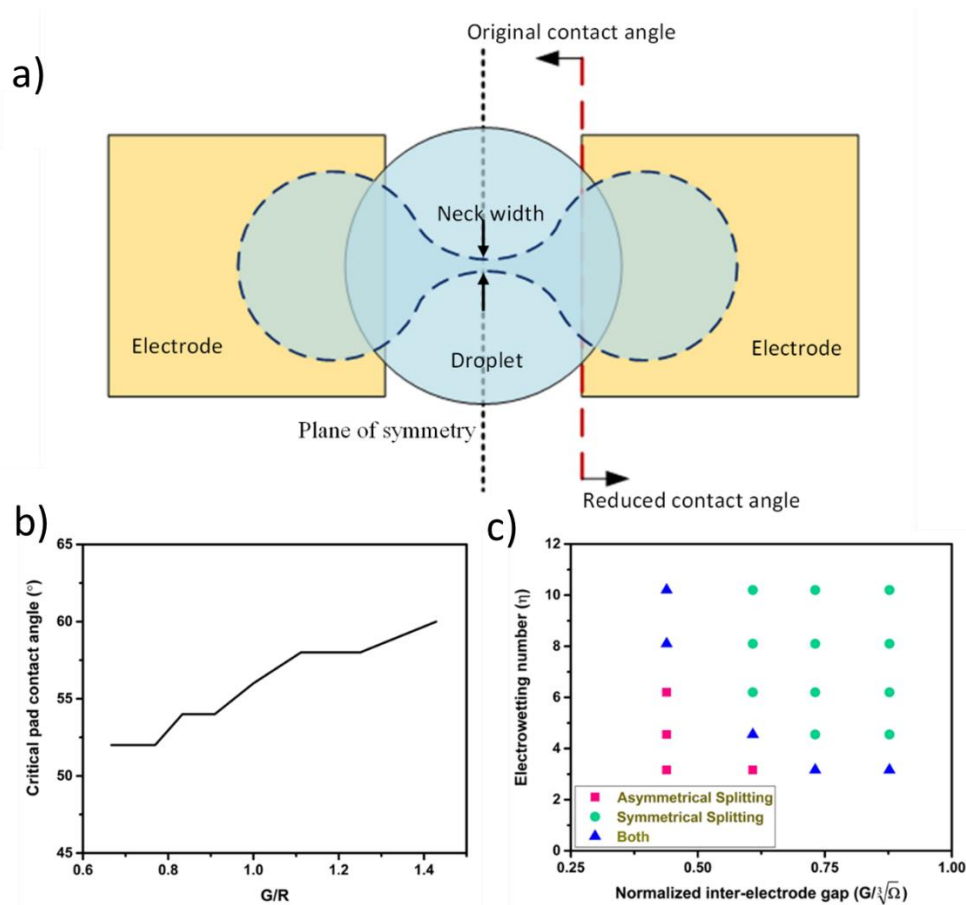
Figure 11: Single-sided splitting of the droplet. Reprinted with permission from ref [119]. Copyright 2022 Wiley-VCH GmbH. (a) Schematic representation of the single-sided splitting of sessile droplets. (b) The critical pad contact angle required for splitting is plotted for different electrode-gap by radius (G/R) ratios. (c) Splitting regimes as a function of electrowetting number ($\eta = cV^2/2\gamma$) and normalized inter-electrode gap ($G/\Omega^{1/3}$, where Ω is the drop volume) for core-shell ratio of 5:1.

Local Interface Actuation for Sensing

Localized electrowetting has been utilized for actuating a part of the droplet interface to sense local liquid properties by tracking changes in interface dynamics. The droplet contact line behaves as a micro-mechanical resonator.[120] Bansal et al.[47] studied the oscillation of a small

droplet interface by actuating it using patterned line electrodes of 50-450 μm width, as shown in Figures 12(a) and (b). Parameters of the actuated liquid interface, like displacement and relaxation time, were investigated to determine the change in the liquid properties of viscosity and surface tension. Such a measurement scheme allows us to estimate the temporal and spatial distribution of material inside complex droplets (e.g., droplet bio-chemical reactors, droplet cell culture mediums, etc.).
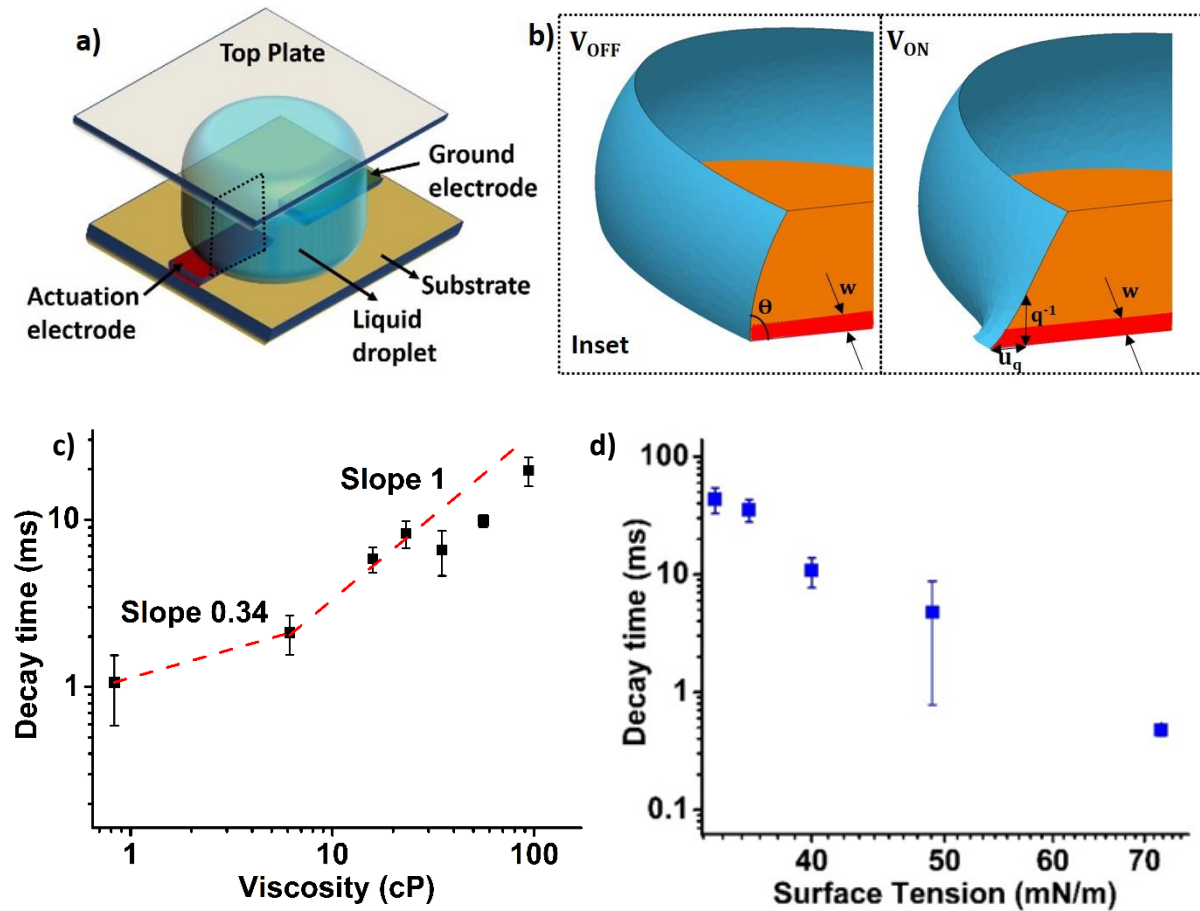

Figure 12: Local interface actuation. Reprinted with permission from ref [47]. Copyright 2020 Elsevier B.V. (a) Schematic of sandwich droplet setup for localized sensing. (b) (right) simulation results showing the stretched interface during local actuation by localized electrowetting. (c) interface relaxation or decay time v/s viscosity plotted for glycerol solutions (viscosity range 0.83 cP- 94 cP). Actuation was by 75 V DC pulse on a 200 μm electrode width. The dashed red line shows guidelines with slopes of 0.34 and 1 for visco-inertial and viscous regimes, respectively. (d) interface relaxation time vs surface tension plotted for DI water and Tween 20 solutions (surface tension ranging from 34 mN/m to 72 mN/m). Actuation was by 75 V DC pulse on a 200 μm electrode width.

The dynamics of the perturbed interface are determined by the balance of surface, inertial and viscous forces. Depending on the relative importance of the three forces, different dependence of relaxation time τ (or characteristic frequency ω) on wavenumber (q), viscosity (μ), and surface tension (γ) are obtained. In a viscous-dominated flow regime, the dynamics are determined by a balance of surface force $F_s \sim \gamma \theta^2 q u_q$ (where θ is the local contact angle and u_q

is the deformation amplitude) and viscous forces $F_v \sim 3\mu l U/\theta$ (where U is the contact line velocity). The characteristic frequency scales as $\omega \sim q\gamma/\mu$. Similarly, in the inertial regime, surface forces are balanced by inertia and an undamped response with a characteristic frequency of $\omega \sim (\gamma\theta/\rho)^{0.5}q^{1.5}$ is obtained. In between these regimes, the visco-inertial regime is observed with a dispersion relation of $\omega \sim (\gamma^2\theta^4/\mu\rho)^{0.33}q^{1.33}$.

For the regime of electrode design, Bansal et al. observed viscous or visco-inertial regimes.[47] The decay time of the actuated interface increased with an increase in liquid viscosity, as seen in Figure 12 (c). At lower viscosities, the relation time shows a visco-inertial behavior ($\tau \propto \mu^{0.33}$). At higher viscosity, a viscous regime is observed with $\tau \propto \mu$. The decay time increases with a decrease in surface tension, as seen in Figure 12(d). This technique has a great potential to sense particles and determine the progress of reactions in both droplet-based platforms and microfluidic channels at different time instants and positions. Continuous change of droplet properties during sugar dissolution and blood coagulation was demonstrated. Table 2 summarizes the various techniques for droplet-based operations.

Table 2: Comparison of different techniques for droplet splitting, generation, migration, and non-coalescence for both in-channel and out-channel devices.

Techniques	In-Channel/Out of Channel Device	Advantages	Limitation	References
Droplet Splitting				
Electrowetting	Out-of-channel	Simple electrode design	Surface needs to hydrophobic	49,119
Surface acoustic wave	Out-of-channel	Inter-digitated electrode design;	Costly fabrication	121
Magnetic actuation	Out-of-channel	Simple actuation	Requires magnetic particles in the droplet, Controllability,	122
Dielectrowetting	Out-of-channel	Simple electrode, work for conductive and non-conductive liquids, no top plate	Residual satellite droplet generation	123
Hydrodynamic technique	In channel	No additional techniques requirement	Geometry specific	124
Droplet impact	Out-of-channel	Quick, reduced contact time with substrate	Only works for specially designed surface	125,126
Droplet Generation/Dispensing				
Electric	In channel	Small response time Large yield	Electrode fouling	127,128
	Out-of-channel	Large yield	High Voltage, heating of droplet	64,72
Light	In channel	Accuracy	Heating, evaporation, Not suitable for bio samples	129

Surface acoustic wave	In channel	Small-size droplets, switchable transition	Complex and costly	130,131
	Out-of-channel	Small size droplets	Costly, polydispersity	34,132
Impact of Droplet	Out-of-channel	Simple & cost-effective, No power consumption	Substrate wettability dependence	84,92,101
Magnetic	In channel	Switchable transition, No thermal effect, Contact less	Fluid property dependence	133,134
	Out-of-channel	Simple technique, Contact less	Fluid property and substrate dependence, Poor droplet size control	135
Geometry	In channel	Fast, high throughput	Optimization, merging	13,15
Droplet Migration				
Geometry	In channel	No use of power	Design dependence, merging	136,137
	Out-of-channel	No use of power	Design and Substrate wettability dependence, slow	138–140
Electric	In channel	Faster response	Not suitable for cell studies for higher electric fields	141
	Out-of-channel	Controlled, faster	Specially designed surface	49,119
Light	In channel	Simple, faster	Surface dependence	142
	Out-of-channel	Simple	Evaporation, controllability	52–54
Magnetic	In channel	Simple actuation	Fluid property dependence or magnetic particles needed	143
	Out-of-channel	Simple setup	Special magnet responsive surface/fluid/particles required	144
Droplet Non-coalescence				
Particle coating	Out-of-channel	Substrate independent, Non-stick, Robust	Limited access to inner material, hydrophobic particles	39,145
	In-channel	Surfactant free, Robust	Low throughput	146
Electrowetting	Out-of-channel	Controllability, prolonged non-coalescence	Works for oil coated droplets only, Hysteresis effects	48,118
Surfactant	In-channel	Simple	Short duration, changes surface tension	147

Conclusion and Outlook

We have discussed the recent advances in droplet generation and manipulation techniques. The generation of monodisperse small droplets with sizes less than 10 µm always remains

challenging due to the dominance of surface tension on the microscale regime. A unique phenomenon of microscale droplet generation and streaming was observed in L-DEP.[55] This intriguing observation was explained as a charge-induced condensation.[63] The electric field penetrates the droplet for an actuation regime of high voltage and high frequency (> 10 kHz). The electric current through the droplet results in Joule heating.[49] Such direct heating of droplets finds applications in biochemical reactions on chips and deicing.[48] The large electric fields used in L-DEP result in soft dielectric breakdown. The ejected charges act as nucleation sites for condensation within the vapor field of the primary droplet. The condensed microdroplets flow in the vapor's convection current leading to the observation of droplet streams.

Generation and maneuvering of micron-sized droplets are crucial for many applications. Due to its micron-scale diameter, the generation of these droplets is of significant interest in the field of aerosol formation, bio & chemical reactions, micro/nanoparticle synthesis, and thermal management for cooling electronic devices. Droplet generation and transport are also studied as pathogen carriers in biology. The charge-induced condensation-based technique is suitable for use in the generation of a large array of small (< 10 µm) droplets. However, there is no control over the position of the droplet stream. It is primarily determined by the convection current. This technique can be extended to droplet-based printing if techniques are developed to control the positioning of the generated droplets. Position control can be achieved through external forces (such as electrostatic) or through controlling the convection stream through flow-focusing structures. Both approaches require fundamental studies to understand the flow behavior and engineering efforts to develop the control structures.

A drop impact technique has been reported for the generation of slightly larger droplets. A droplet impacting a nanostructured superhydrophobic sieve leads to the ejection of a liquid jet through the sieve pore. For jets longer than their diameter, given sufficient time, the jet breaks into droplets.[67] Interestingly, a low impact velocity impact regime has been reported where jet ejection has been observed during the recoil phase of the droplet impact. This anomalous ejection and subsequent droplet creation have been attributed to the collapse of a cavity formed during the droplet impact.[88] This regime has been exploited to demonstrate a versatile drop-on-demand printing technique. This technique can print liquids with very high mass loading as clogging is eliminated due to the absence of a nozzle.

Conventional drop generation on-demand-based has been used for decades. The requirement for particular applications drove the development of these printers. For example, acoustophoretic printers are best suited to print viscous materials for biological applications (e.g. Matrigel). Likewise, electrohydrodynamic printers are used for high-resolution printing. The long-standing common drawback of these techniques was the inability to print high mass-loaded solutions. Drop impact printing has addressed this drawback by enabling high mass-loading printing. However, drop-impact printing has low throughput, and the recyclability of ink is a concern. These shortcomings can be addressed in the future by introducing other forces (e.g., electrostatic, acoustic, etc.) and mechanisms to actuate liquid droplets.

A further possibility of ejection of many droplets at higher impact velocity has also been explored.[100] Several interesting phenomena have been observed. Firstly, an onset of pancake bouncing is observed for meshes with low anti-penetration pressure. This has been attributed to the kinetic energy of the recoiling interface after the jet breakage. Secondly, the loss of mass through the droplet ejection reduces contact time as the effective droplet radius is reduced. Thirdly, the flexibility of the mesh leads to pancake bouncing with reduced contact time. In all impact-based droplet generation techniques, only a small fraction of the primary droplet is used. The rest of the droplet needs to be recycled. This is a major problem that still needs to be resolved. Further, application-specific improvements and optimizations need to be carried out.

With a vision to enable better integration of various sensors and actuators, an open-chip EWOD platform has been developed. Several challenges in fundamental droplet operations, such as splitting, merging, and mixing, have hindered the advance of an open-chip platform. Contamination and evaporation have also been a concern. Over the past few years, several advancements have been made toward addressing these concerns. An oil-covered compound droplet scheme has been developed to address the evaporation and contamination issues.[40] Merging of compound droplets is slowed down due to the presence of an oil bridge. EWOD actuation was investigated to enable rapid mixing.[42] Interestingly, two different regimes of rapid coalescence and prolonged non-coalescence were observed. Both regimes are interesting for different applications. Splitting bare droplets using electrowetting forces has been difficult.

A recent study has evaluated the critical contact angle required for open-chip splitting.[116] Contact angle saturation limits the low contact angles required for open chip splitting. Compound droplets have been demonstrated as a solution. The thin oil layer between the substrate and the droplet eases droplet motion by reducing contact angle hysteresis. It further

helps form a cylindrical liquid bridge suspended in oil. In contrast to a sessile bridge, a suspended bride easily breaks due to Rayleigh-Plateau instability. Finally, a local interface actuation has been used to sense droplets' local fluid properties.[41] Tracking of temporal and spatial changes in the fluid properties has been demonstrated. Despite several advancements, the adoption of droplet-based microfluidic devices has been limited. Further advances in the integration of various sensors will open up opportunities for droplet-based platforms in different applications.

Since the droplet-based device is suitable for automated sample preparation for assays while the channel-based approach is good for single-cell analysis applications, this work would provide a new direction for developing integrated lab-on-chip devices. The open configuration would provide easy accessibility of droplets, better integration of detection techniques, and can be integrated with channel-based devices efficiently. Though droplet oscillation and manipulation studies offer promising futuristic applications, many non-linear phenomena like damping and hysteresis have been neglected or simplified in the literature, restricting their broad applicability in real-life scenarios. The role of these non-linear characteristics can be analyzed to gain more valuable insights into droplet behavior and its dynamics for real-world applications. The localized electrowetting technique for open chip sensing can be combined with microfluidic channels to determine a fluid's temporal or spatial state or for particle/cell sensing. Such cross-disciplinary approaches and compact sensor designs have potential applications in building point-of-care systems and lab-on-chip devices.

Depending on the method used, the techniques described in this article are suitable for generating and manipulating both single and multiple droplets. The charge-induced condensation-based droplet generation technique is better suited for multi-droplet generation. The generation rate of the charge is controllable to some extent by the applied voltage. However, the control is not sufficient to enable single droplet generation. In contrast, the drop impact technique is suitable for both single and multi-droplet generation. EWOD generally manipulates one droplet at a time. However, EWOD enables electrode designs where multiple droplets can be manipulated in parallel.

References:

(1) Joung, Y. S.; Buie, C. R. Aerosol Generation by Raindrop Impact on Soil. *Nature Communications 2015 6:1* **2015**, *6* (1), 1–9. https://doi.org/10.1038/ncomms7083.

(2) Joung, Y. S.; Ge, Z.; Buie, C. R. Bioaerosol Generation by Raindrops on Soil. *Nature Communications 2017 8:1* **2017**, *8* (1), 1–10. https://doi.org/10.1038/ncomms14668.

(3) Taniguchi, T.; Torii, T.; Higuchi, T. Chemical Reactions in Microdroplets by Electrostatic Manipulation of Droplets in Liquid Media. *Lab Chip* **2002**, *2* (1), 19–23. https://doi.org/10.1039/B108739H.

(4) Tsuji, K.; Müller, S. C. Chemical Reaction Evolving on a Droplet. *Journal of Physical Chemistry Letters* **2012**, *3* (8), 977–980. https://doi.org/10.1021/JZ300227Q/SUPPL_FILE/JZ300227Q_SI_001.PDF.

(5) Rastogi, V.; Garcia, A. A.; Marquez, M.; Velev, O. D. Anisotropic Particle Synthesis Inside Droplet Templates on Superhydrophobic Surfaces. *Macromol Rapid Commun* **2010**, *31* (2), 190–195. https://doi.org/10.1002/MARC.200900587.

(6) Millman, J. R.; Bhatt, K. H.; Prevo, B. G.; Velev, O. D. Anisotropic Particle Synthesis in Dielectrophoretically Controlled Microdroplet Reactors. *Nature Materials 2004 4:1* **2004**, *4* (1), 98–102. https://doi.org/10.1038/nmat1270.

(7) Bindiganavale, G. S.; Amaya, M.; Moon, H. Demonstration of Hotspot Cooling Using Digital Microfluidic Device. *Journal of Micromechanics and Microengineering* **2018**, *28* (12), 125015. https://doi.org/10.1088/1361-6439/AAE883.

(8) Oh, J.; Birbarah, P.; Foulkes, T.; Yin, S. L.; Rentauskas, M.; Neely, J.; Pilawa-Podgurski, R. C. N.; Miljkovic, N. Jumping-Droplet Electronics Hot-Spot Cooling. *Appl Phys Lett* **2017**, *110* (12), 123107. https://doi.org/10.1063/1.4979034.

(9) Mukherjee, R.; Gruszewski, H. A.; Bilyeu, L. T.; Schmale, D. G.; Boreyko, J. B. Synergistic Dispersal of Plant Pathogen Spores by Jumping-Droplet Condensation and Wind. *Proc Natl Acad Sci U S A* **2021**, *118* (34), e2106938118. https://doi.org/10.1073/PNAS.2106938118/SUPPL_FILE/PNAS.2106938118.SM02.MP4.

(10) Kim, S.; Park, H.; Gruszewski, H. A.; Schmale, D. G.; Jung, S. Vortex-Induced Dispersal of a Plant Pathogen by Raindrop Impact. *Proc Natl Acad Sci U S A* **2019**, *116* (11), 4917–4922. https://doi.org/10.1073/PNAS.1820318116.

(11)   Hoath, S. D. *Fundamentals of Inkjet Printing: The Science of Inkjet and Droplets*; John Wiley & Sons, 2016.

(12)   Li, J.; Rossignol, F.; Macdonald, J. Inkjet Printing for Biosensor Fabrication: Combining Chemistry and Technology for Advanced Manufacturing. *Lab Chip* **2015**, *15* (12), 2538–2558.

(13)   Zhu, P.; Wang, L. Passive and Active Droplet Generation with Microfluidics: A Review. *Lab Chip* **2016**, *17* (1), 34–75. https://doi.org/10.1039/C6LC01018K.

(14)   Chong, Z. Z.; Tan, S. H.; Gañán-Calvo, A. M.; Tor, S. B.; Loh, N. H.; Nguyen, N. T. Active Droplet Generation in Microfluidics. *Lab Chip* **2015**, *16* (1), 35–58. https://doi.org/10.1039/C5LC01012H.

(15)   Utada, A. S.; Fernandez-Nieves, A.; Stone, H. A.; Weitz, D. A. Dripping to Jetting Transitions in Coflowing Liquid Streams. *Phys Rev Lett* **2007**, *99* (9), 094502. https://doi.org/10.1103/PHYSREVLETT.99.094502/FIGURES/4/MEDIUM.

(16)   Hemachandran, E.; Hoque, S. Z.; Laurell, T.; Sen, A. K. Reversible Stream Drop Transition in a Microfluidic Coflow System via On Demand Exposure to Acoustic Standing Waves. **2021**. https://doi.org/10.1103/PhysRevLett.127.134501.

(17)   Feng, H.; Zheng, T.; Li, M.; Wu, J.; Ji, H.; Zhang, J.; Zhao, W.; Guo, J. Droplet-Based Microfluidics Systems in Biomedical Applications. *Electrophoresis* **2019**, *40* (11), 1580–1590. https://doi.org/10.1002/ELPS.201900047.

(18)   Ling, S. da; Geng, Y.; Chen, A.; Du, Y.; Xu, J. Enhanced Single-Cell Encapsulation in Microfluidic Devices: From Droplet Generation to Single-Cell Analysis. *Biomicrofluidics* **2020**, *14* (6), 061508. https://doi.org/10.1063/5.0018785.

(19)   Shi, Z.; Lai, X.; Sun, C.; Zhang, X.; Zhang, L.; Pu, Z.; Wang, R.; Yu, H.; Li, D. Step Emulsification in Microfluidic Droplet Generation: Mechanisms and Structures. *Chemical Communications* **2020**, *56* (64), 9056–9066. https://doi.org/10.1039/D0CC03628E.

(20)   Chen, Z.; Kheiri, S.; Young, E. W. K.; Kumacheva, E. Trends in Droplet Microfluidics: From Droplet Generation to Biomedical Applications. *Langmuir* **2022**. https://doi.org/10.1021/ACS.LANGMUIR.2C00491/ASSET/IMAGES/LARGE/LA2C00491_0004.JPEG.

(21)   Bradbury, R. Thermal Printing. In *Chemistry and Technology of printing and imaging systems*; Springer, 1996; pp 139–167.

(22)   Foresti, D.; Kroll, K. T.; Amissah, R.; Sillani, F.; Homan, K. A.; Poulikakos, D.; Lewis, J. A. Acoustophoretic Printing. *Sci Adv* **2018**, *4* (8), eaat1659.

(23)   Han, Y.; Dong, J. Electrohydrodynamic Printing for Advanced Micro/Nanomanufacturing: Current Progresses, Opportunities, and Challenges. *J Micro Nanomanuf* **2018**, *6* (4), 1–20. https://doi.org/10.1115/1.4041934.

(24)   Singh, M.; Haverinen, H. M.; Dhagat, P.; Jabbour, G. E. Inkjet Printing—Process and Its Applications. *Advanced materials* **2010**, *22* (6), 673–685.

(25)   Nallan, H. C.; Sadie, J. A.; Kitsomboonloha, R.; Volkman, S. K.; Subramanian, V. Systematic Design of Jettable Nanoparticle-Based Inkjet Inks: Rheology, Acoustics, and Jettability. *Langmuir* **2014**, *30* (44), 13470–13477. https://doi.org/10.1021/la502903y.

(26) Lepowsky, E.; Muradoglu, M.; Tasoglu, S. Towards Preserving Post-Printing Cell Viability and Improving the Resolution: Past, Present, and Future of 3D Bioprinting Theory. *Bioprinting* **2018**, *11*, e00034.

(27) Yusof, A.; Keegan, H.; Spillane, C. D.; Sheils, O. M.; Martin, C. M.; O'Leary, J. J.; Zengerle, R.; Koltay, P. Inkjet-like Printing of Single-Cells. *Lab Chip* **2011**, *11* (14), 2447–2454.

(28) Lee, A.; Sudau, K.; Ahn, K. H.; Lee, S. J.; Willenbacher, N. Optimization of Experimental Parameters to Suppress Nozzle Clogging in Inkjet Printing. *Ind Eng Chem Res* **2012**, *51* (40), 13195–13204.

(29) Lohse, D. Fundamental Fluid Dynamics Challenges in Inkjet Printing. *Annu Rev Fluid Mech* **2022**, *54*, 349–382.

(30) Xu, B.; Chen, X.; Zhao, | He; Zhang, Z.; Liu, H. Preparation of Nano-Pico Droplets Using an Open Fibrous System. *Droplet* **2022**, e27. https://doi.org/10.1002/DRO2.27.

(31) Ferraro, P.; Coppola, S.; Grilli, S.; Paturzo, M.; Vespini, V. Dispensing Nano–Pico Droplets and Liquid Patterning by Pyroelectrodynamic Shooting. *Nature Nanotechnology 2010 5:6* **2010**, *5* (6), 429–435. https://doi.org/10.1038/nnano.2010.82.

(32) Dung Luong, T.; Trung Nguyen, N. Surface Acoustic Wave Driven Microfluidics – A Review. *Micro and Nanosystemse* **2012**, *2* (3), 217–225. https://doi.org/10.2174/1876402911002030217.

(33) Lei, Y.; Hu, H. SAW-Driven Droplet Jetting Technology in Microfluidic: A Review. *Biomicrofluidics* **2020**, *14* (6), 061505. https://doi.org/10.1063/5.0014768.

(34) Nampoothiri, K. N.; Satpathi, N. S.; Sen, A. K. Surface Acoustic Wave-Based Generation and Transfer of Droplets onto Wettable Substrates. *RSC Adv* **2022**, *12* (36), 23400–23410. https://doi.org/10.1039/D2RA04089A.

(35) Emanetoglu, N. W.; Gorla, C.; Liu, Y.; Liang, S.; Lu, Y. Epitaxial ZnO Piezoelectric Thin Films for Saw Filters. *Mater Sci Semicond Process* **1999**, *2* (3), 247–252. https://doi.org/10.1016/S1369-8001(99)00022-0.

(36) Garstecki, P.; Kaminski, S. T. S.; Garstecki, P.; Kaminski, T. S. Controlled Droplet Microfluidic Systems for Multistep Chemical and Biological Assays. *Chem Soc Rev* **2017**, *46* (20), 6210–6226. https://doi.org/10.1039/C5CS00717H.

(37) Shang, L.; Cheng, Y.; Zhao, Y. Emerging Droplet Microfluidics. *Chem Rev* **2017**, *117* (12), 7964–8040. https://doi.org/10.1021/ACS.CHEMREV.6B00848/ASSET/IMAGES/ACS.CHEMREV.6B00848.SOCIAL.JPEG_V03.

(38) Lathia, R.; Sen, P. JMEMS Letters Fabrication of Self-Sealed Circular Microfluidic Channels in Glass by Thermal Blowing Method. *Journal of Microelectromechanical Systems* **2022**, *31* (2), 177–179. https://doi.org/10.1109/JMEMS.2021.3135459.

(39) Lathia, R.; Sen, P. Sol–Gel-Derived Nanoparticles Coated Liquid Entities: Liquid Marbles, Liquid Plasticine, and Flat Interface. *Journal of Micromechanics and Microengineering* **2022**, *33* (2), 024002. https://doi.org/10.1088/1361-6439/ACAD89.

(40) Barman, S. R.; Khan, I.; Chatterjee, S.; Saha, S.; Choi, D.; Lee, S.; Lin, Z. H. Electrowetting-on-Dielectric (EWOD): Current Perspectives and Applications in Ensuring Food Safety. *J Food Drug Anal* **2020**, *28* (4), 596–622. https://doi.org/10.38212/2224-6614.1239.

(41) Rui, X.; Song, S.; Wang, W.; Zhou, J. Applications of Electrowetting-on-Dielectric (EWOD) Technology for Droplet Digital PCR. *Biomicrofluidics* **2020**, *14* (6), 061503. https://doi.org/10.1063/5.0021177.

(42) Nelson, W. C.; Kim, C. J. C. Droplet Actuation by Electrowetting-on-Dielectric (EWOD): A Review. *J Adhes Sci Technol* **2012**, *26* (12–17), 1747–1771. https://doi.org/10.1163/156856111X599562.

(43) Zhu, G. P.; Wang, Q. Y.; Ma, Z. K.; Wu, S. H.; Guo, Y. P. Droplet Manipulation under a Magnetic Field: A Review. *Biosensors 2022, Vol. 12, Page 156* **2022**, *12* (3), 156. https://doi.org/10.3390/BIOS12030156.

(44) Choi, K.; Ng, A. H. C.; Fobel, R.; Wheeler, A. R. Digital Microfluidics. *Annual Review of Analytical Chemistry* **2012**, *5* (1), 413–440. https://doi.org/10.1146/annurev-anchem-062011-143028.

(45) Bansal, S.; Subramanian, S. A Microfluidic Acoustic Metamaterial Using Electrowetting: Enabling Active Broadband Tunability. *Adv Mater Technol* **2021**, *2100491*. https://doi.org/10.1002/admt.202100491.

(46) Bansal, S.; Sen, P. Axisymmetric and Nonaxisymmetric Oscillations of Sessile Compound Droplets in an Open Digital Microfluidic Platform. *Langmuir* **2017**, *33* (41), 11047–11058. https://doi.org/10.1021/acs.langmuir.7b02042.

(47) Bansal, S.; Sen, P. Electrowetting Based Local Sensing of Liquid Properties Using Relaxation Dynamics of Stretched Liquid Interface. *J Colloid Interface Sci* **2020**, *568*, 8–15. https://doi.org/10.1016/j.jcis.2020.02.035.

(48) Bansal, S.; Sen, P. Effect of Electrowetting Induced Capillary Oscillations on Coalescence of Compound Droplets. *J Colloid Interface Sci* **2018**, *530*, 223–232.

(49) Sung Kwon Cho; Hyejin Moon; Chang-Jin Kim. Creating, Transporting, Cutting, and Merging Liquid Droplets by Electrowetting-Based Actuation for Digital Microfluidic Circuits. *Journal of Microelectromechanical Systems* **2003**, *12* (1), 70–80. https://doi.org/10.1109/jmems.2002.807467.

(50) Bansal, S.; Tokuda, Y.; Peasley, J.; Subramanian, S. Electrically Induced Liquid Metal Droplet Bouncing. *Langmuir* **2022**. https://doi.org/10.1021/acs.langmuir.2c00577.

(51) Bansal, S.; Sen, P. Mixing Enhancement by Degenerate Modes in Electrically Actuated Sessile Droplets. *Sens Actuators B Chem* **2016**, *232*, 318–326. https://doi.org/10.1016/J.SNB.2016.03.109.

(52) Kavokine, N.; Anyfantakis, M.; Morel, M.; Rudiuk, S.; Bickel, T.; Baigl, D. Light-Driven Transport of a Liquid Marble with and against Surface Flows. *Angewandte Chemie - International Edition* **2016**, *55* (37), 11183–11187. https://doi.org/10.1002/anie.201603639.

(53) Yan, W.; Zhao, C.; Luo, W.; Zhang, W.; Li, X.; Liu, D. Optically Guided Pyroelectric Manipulation of Water Droplet on a Superhydrophobic Surface. *ACS Appl Mater Interfaces*

2021, *13* (19), 23181–23190.
https://doi.org/10.1021/ACSAMI.1C03407/SUPPL_FILE/AM1C03407_SI_012.AVI.

(54)   Xu, W.; Song, Y.; Xu, R. X.; Wang, Z. Electrohydrodynamic and Hydroelectric Effects at the Water–Solid Interface: From Fundamentals to Applications. *Adv Mater Interfaces* **2021**, *8* (2), 2000670. https://doi.org/10.1002/ADMI.202000670.

(55)   Qian, C.; Zhou, F.; Wang, T.; Li, Q.; Hu, D.; Chen, X.; Wang, Z. Pancake Jumping of Sessile Droplets. *Advanced Science* **2022**, *9* (7), 2103834. https://doi.org/10.1002/ADVS.202103834.

(56)   Satpathi, N. S.; Malik, L.; Ramasamy, A. S.; Sen, A. K. Drop Impact on a Superhydrophilic Spot Surrounded by a Superhydrophobic Surface. *Langmuir* **2021**, *37* (48), 14195–14204. https://doi.org/10.1021/ACS.LANGMUIR.1C02654/ASSET/IMAGES/MEDIUM/LA1C02654_M0 15.GIF.

(57)   Jones, T. B. Liquid Dielectrophoresis on the Microscale. *J Electrostat* **2001**, *51–52* (1–4), 290–299. https://doi.org/10.1016/S0304-3886(01)00074-2.

(58)   Kaler, K. V. I. S.; Prakash, R.; Chugh, D. Liquid Dielectrophoresis and Surface Microfluidics. *Biomicrofluidics* **2010**, *4* (2), 022805. https://doi.org/10.1063/1.3411003.

(59)   Nampoothiri, K. N.; Bobji, M. S.; Sen, P. De-Icing Device With Self-Adjusting Power Consumption and Ice Sensing Capabilities. *Journal of Microelectromechanical Systems* **2020**, *29* (4), 562–570. https://doi.org/10.1109/jmems.2020.3004502.

(60)   Nampoothiri, K. N.; Seshasayee, M. S.; Srinivasan, V.; Bobji, M. S.; Sen, P. Direct Heating of Aqueous Droplets Using High Frequency Voltage Signals on an EWOD Platform. *Sens Actuators B Chem* **2018**, *273* (June), 862–872. https://doi.org/10.1016/j.snb.2018.06.091.

(61)   Nampoothiri, K. N.; Sen, P. Motion of Generated Dumbbell-Shaped Satellite Droplets during Liquid Dielectrophoresis. *Journal of Micromechanics and Microengineering* **2021**, *31* (9). https://doi.org/10.1088/1361-6439/ac1845.

(62)   Kanagasabapathi, T. T.; Kaler, K. V. I. S. Surface Microfluidics - High-Speed DEP Liquid Actuation on Planar Substrates and Critical Factors in Reliable Actuation. *Journal of Micromechanics and Microengineering* **2007**, *17* (4), 743–752. https://doi.org/10.1088/0960-1317/17/4/011.

(63)   Chen, C.; Tsai, S.; Jang, L. Droplet Creation Using Liquid Dielectrophoresis. *Sens Actuators B Chem* **2009**, *142* (1), 369–376. https://doi.org/10.1016/j.snb.2009.08.001.

(64)   Nampoothiri, K. N.; Srinivasan, V.; Bobji, M. S.; Sen, P. A Novel Sub-Picoliter Monodispersed Droplet Generation Device Based on Liquid Dielectrophoresis. In *2017 IEEE 30th International Conference on Micro Electro Mechanical Systems (MEMS)*; IEEE, 2017; pp 87–90. https://doi.org/10.1109/MEMSYS.2017.7863346.

(65)   Ko, S. H.; Lee, H.; Kang, K. H. Hydrodynamic Flows in Electrowetting. *Langmuir* **2008**, *24* (3), 1094–1101. https://doi.org/10.1021/la702455t.

(66)   García-Sánchez, P.; Ramos, A.; Mugele, F. Electrothermally Driven Flows in Ac Electrowetting. *Phys Rev E* **2010**, *81* (1), 015303. https://doi.org/10.1103/PhysRevE.81.015303.

(67)   Lee, H.; Yun, S.; Ko, S. H.; Kang, K. H. An Electrohydrodynamic Flow in Ac Electrowetting. *Biomicrofluidics* **2009**, *3* (4), 044113. https://doi.org/10.1063/1.3274511.

(68)   Samiei, E.; de Leon Derby, M. D.; den Berg, A. van; Hoorfar, M. An Electrohydrodynamic Technique for Rapid Mixing in Stationary Droplets on Digital Microfluidic Platforms. *Lab Chip* **2017**, *17* (2), 227–234. https://doi.org/10.1039/C6LC00997B.

(69)   Issadore, D.; Humphry, K. J.; Brown, K. A.; Sandberg, L.; Weitz, D. A.; Westervelt, R. M. Microwave Dielectric Heating of Drops in Microfluidic Devices. *Lab Chip* **2009**, *9* (12), 1701. https://doi.org/10.1039/b822357b.

(70)   Ramos, A.; Morgan, H.; Green, N. G.; Castellanos, A. Ac Electrokinetics: A Review of Forces in Microelectrode Structures. *J Phys D Appl Phys* **1999**, *31* (18), 2338–2353. https://doi.org/10.1088/0022-3727/31/18/021.

(71)   Green, N. G.; Ramos, A.; González, A.; Castellanos, A.; Morgan, H. Electrothermally Induced Fluid Flow on Microelectrodes. *J Electrostat* **2001**, *53* (2), 71–87. https://doi.org/10.1016/S0304-3886(01)00132-2.

(72)   Nampoothiri, K. N.; Bobji, M. S.; Sen, P. Generation of Micron-Sized Droplet Streams by High Frequency Electric Fields. *Int J Heat Mass Transf* **2019**, *145*, 118709. https://doi.org/10.1016/j.ijheatmasstransfer.2019.118709.

(73)   Yang, Y.; Tan, X.; Liu, D.; Lu, X.; Zhao, C.; Lu, J.; Pan, Y. Corona Discharge-Induced Rain and Snow Formation in Air. *IEEE Transactions on Plasma Science* **2018**, *46* (5), 1786–1792. https://doi.org/10.1109/TPS.2018.2820200.

(74)   Reznikov, M. Electrically Enhanced Condensation I: Effects of Corona Discharge. *IEEE Trans Ind Appl* **2015**, *51* (2), 1137–1145. https://doi.org/10.1109/TIA.2014.2354734.

(75)   Ju, J.; Wang, T. J.; Li, R.; Du, S.; Sun, H.; Liu, Y.; Tian, Y.; Bai, Y.; Liu, Y.; Chen, N.; Wang, J.; Wang, C.; Liu, J.; Chin, S. L.; Xu, Z. Corona Discharge Induced Snow Formation in a Cloud Chamber. *Sci Rep* **2017**, *7* (1), 3–7. https://doi.org/10.1038/s41598-017-12002-5.

(76)   Pan, Z.; Dash, S.; Weibel, J. A.; Garimella, S. v. Assessment of Water Droplet Evaporation Mechanisms on Hydrophobic and Superhydrophobic Substrates. *Langmuir* **2013**, *29* (51), 15831–15841. https://doi.org/10.1021/la4045286.

(77)   Modak, C. D.; Bhaumik, S. K. Creeping Flow Dynamics over Superhydrophobic Ball: Slip Effects and Drag Reduction. *Colloids Surf A Physicochem Eng Asp* **2017**, *529*, 998–1008.

(78)   Geyer, F.; D'Acunzi, M.; Sharifi-Aghili, A.; Saal, A.; Gao, N.; Kaltbeitzel, A.; Sloot, T.-F.; Berger, R.; Butt, H.-J.; Vollmer, D. When and How Self-Cleaning of Superhydrophobic Surfaces Works. *Sci Adv* **2020**, *6* (3), eaaw9727.

(79)   Haechler, I.; Park, H.; Schnoering, G.; Gulich, T.; Rohner, M.; Tripathy, A.; Milionis, A.; Schutzius, T. M.; Poulikakos, D. Exploiting Radiative Cooling for Uninterrupted 24-Hour Water Harvesting from the Atmosphere. *Sci Adv* **2021**, *7* (26), eabf3978.

(80)   Hou, Y.; Peng, Z.; Liang, J.; Fu, S. Facile Preparation of Petaliform-like Superhydrophobic Meshes via Moisture Etching for Oil-Water Separation. *Surf Coat Technol* **2020**, *399*, 126124.

(81)   Ma, C.; Chen, L.; Wang, L.; Tong, W.; Chu, C.; Yuan, Z.; Lv, C.; Zheng, Q. Condensation Droplet Sieve. *Nat Commun* **2022**, *13* (1), 5381. https://doi.org/10.1038/s41467-022-32873-1.

(82)   Sun, L.; Lin, S.; Pang, B.; Wang, Y.; Li, E.; Zu, X.; Zhang, K.; Xiang, X.; Chen, L. Water Sprays Formed by Impinging Millimeter-Sized Droplets on Superhydrophobic Meshes. *Physics of Fluids* **2021**, *33* (9), 092111.

(83)   Kumar, A.; Tripathy, A.; Raj, S.; Sen, P. Significant Reduction in Droplet Ejection for Terminal Velocity Impact Using a Combination of Superhydrophilic & Superhydrophobic Sieve. In *2018 IEEE Micro Electro Mechanical Systems (MEMS)*; IEEE, 2018; pp 257–260.

(84)   Kumar, A.; Tripathy, A.; Modak, C. D.; Sen, P. Designing Assembly of Meshes Having Diverse Wettability for Reducing Liquid Ejection at Terminal Velocity Droplet Impact. *Journal of Microelectromechanical Systems* **2018**, *27* (5), 866–873. https://doi.org/10.1109/JMEMS.2018.2850903.

(85)   Yong, J.; Chen, F.; Li, W.; Huo, J.; Fang, Y.; Yang, Q.; Bian, H.; Hou, X. Underwater Superaerophobic and Superaerophilic Nanoneedles-Structured Meshes for Water/Bubbles Separation: Removing or Collecting Gas Bubbles in Water. *Global Challenges* **2018**, *2* (4), 1700133.

(86)   Mehrizi, A. A.; Lin, S.; Sun, L.; Wang, Y.; Chen, L. Penetration and Ligament Formation of Viscoelastic Droplets Impacting on the Superhydrophobic Mesh. *Sci Rep* **2022**, *12* (1), 11920. https://doi.org/10.1038/s41598-022-15645-1.

(87)   Bae, C.; Oh, S.; Han, J.; Nam, Y.; Lee, C. Water Penetration Dynamics through a Janus Mesh during Drop Impact. *Soft Matter* **2020**, *16* (26), 6072–6081.

(88)   Ryu, S.; Sen, P.; Nam, Y.; Lee, C. Water Penetration through a Superhydrophobic Mesh during a Drop Impact. *Phys Rev Lett* **2017**, *118* (1), 014501.

(89)   Raiyan, A.; Mclaughlin, T. S.; Annavarapu, R. K.; Sojoudi, H. Effect of Superamphiphobic Macrotextures on Dynamics of Viscous Liquid Droplets. *Scientific Reports 2018 8:1* **2018**, *8* (1), 1–14. https://doi.org/10.1038/s41598-018-33656-9.

(90)   Biance, A. L.; Chevy, F.; Clanet, C.; Lagubeau, G.; Quéré, D. On the Elasticity of an Inertial Liquid Shock. *J Fluid Mech* **2006**, *554*, 47–66. https://doi.org/10.1017/S0022112006009189.

(91)   CLANET, C.; BÉGUIN, C.; RICHARD, D.; QUÉRÉ, D. Maximal Deformation of an Impacting Drop. *J Fluid Mech* **2004**, *517*, 199–208. https://doi.org/DOI: 10.1017/S0022112004000904.

(92)   Modak, C. D.; Kumar, A.; Tripathy, A.; Sen, P. Drop Impact Printing. *Nature Communications 2020 11:1* **2020**, *11* (1), 1–11. https://doi.org/10.1038/s41467-020-18103-6.

(93)   Castrejon-Pita, J. R.; Baxter, W. R. S.; Morgan, J.; Temple, S.; Martin, G. D.; Hutchings, I. M. FUTURE, OPPORTUNITIES AND CHALLENGES OF INKJET TECHNOLOGIES. *Atomization and Sprays* **2013**, *23* (6), 541–565. https://doi.org/10.1615/AtomizSpr.2013007653.

(94)   Almeida, R.; Kwon, J. W. Nonvolatile Liquid-Film-Embedded Microfluidic Valve for Microscopic Evaporation Control Without Stiction Problem at Liquid–Air Interfaces. *Journal of microelectromechanical systems* **2012**, *21* (4), 981–989.

(95)   Shi, S.; Bai, W.; Xuan, T.; Zhou, T.; Dong, G.; Xie, R. In Situ Inkjet Printing Patterned Lead Halide Perovskite Quantum Dot Color Conversion Films by Using Cheap and Eco-Friendly Aqueous Inks. *Small Methods* **2021**, *5* (3), 2000889.

(96)   Chakraborty, S.; Luchena, C.; Elton, J. J.; Schilling, M. P.; Reischl, M.; Roux, M.; Levkin, P. A.; Popova, A. A. "Cells-to-cDNA on Chip": Phenotypic Assessment and Gene Expression Analysis from Live Cells in Nanoliter Volumes Using Droplet Microarrays. *Adv Healthc Mater* **2022**, 2102493.

(97)   Xie, T.; Zhang, Q.; Zhang, W.; Feng, S.; Lin, J. Inkjet-Patterned Microdroplets as Individual Microenvironments for Adherent Single Cell Culture. *Small* **2022**, *18* (19), 2107992.

(98)   Mu, B.; Xu, Y.; Xu, J.; Nikitina, M. A.; Zafari, U.; Xiao, X. Inkjet Direct Printing Approach for Flexible Electronic. *Results in Engineering* **2022**, *14*, 100466.

(99)   Lejeune, M.; Chartier, T.; Dossou-Yovo, C.; Noguera, R. Ink-Jet Printing of Ceramic Micro-Pillar Arrays. *J Eur Ceram Soc* **2009**, *29* (5), 905–911.

(100)   Alomari, M.; Mohamed, F. H.; Basit, A. W.; Gaisford, S. Personalised Dosing: Printing a Dose of One's Own Medicine. *Int J Pharm* **2015**, *494* (2), 568–577.

(101)   Soto, D.; Girard, H.-L. L.; le Helloco, A.; Binder, T.; Quéré, D.; Varanasi, K. K. Droplet Fragmentation Using a Mesh. *Phys Rev Fluids* **2018**, *3* (8), 1–10. https://doi.org/10.1103/PhysRevFluids.3.083602.

(102)   Kumar, A.; Tripathy, A.; Nam, Y.; Lee, C.; Sen, P. Effect of Geometrical Parameters on Rebound of Impacting Droplets on Leaky Superhydrophobic Meshes. *Soft Matter* **2018**, *14* (9), 1571–1580. https://doi.org/10.1039/c7sm02145c.

(103)   Liu, Y.; Moevius, L.; Xu, X.; Qian, T.; Yeomans, J. M.; Wang, Z. Pancake Bouncing on Superhydrophobic Surfaces. *Nat Phys* **2014**, *10* (7), 515–519. https://doi.org/10.1038/nphys2980.

(104)   Yi, U. C.; Kim, C. J. Characterization of Electrowetting Actuation on Addressable Single-Side Coplanar Electrodes. *Journal of Micromechanics and Microengineering* **2006**, *16* (10), 2053–2059. https://doi.org/10.1088/0960-1317/16/10/018.

(105)   Neeson, M. J.; Tabor, R. F.; Grieser, F.; Dagastine, R. R.; Chan, D. Y. C. Compound Sessile Drops. *Soft Matter* **2012**, *8* (43), 11042–11050. https://doi.org/10.1039/C2SM26637G.

(106)   Daniel, D.; Timonen, J. V. I.; Li, R.; Velling, S. J.; Aizenberg, J. Oleoplaning Droplets on Lubricated Surfaces. *Nature Physics 2017 13:10* **2017**, *13* (10), 1020–1025. https://doi.org/10.1038/nphys4177.

(107)   Rayleigh, L. On the Capillary Phenomena of Jets. *Proceedings of the Royal Society of London* **1879**, *29* (196–199), 71–97. https://doi.org/10.1098/rspl.1879.0015.

(108)   Bostwick, J. B.; Steen, P. H. Dynamics of Sessile Drops. Part 1. Inviscid Theory. *J Fluid Mech* **2014**, *760*, 5–38. https://doi.org/10.1017/JFM.2014.582.

(109)   Sharma, S.; Wilson, D. I. On a Toroidal Method to Solve the Sessile-Drop Oscillation Problem. *J Fluid Mech* **2021**, *919*, A39. https://doi.org/10.1017/JFM.2021.419.

(110)   Lamb, H. Hydrodynamics. *Cambridge University Press* **1932**, *1–8* (6th Edition).

(111)   Noblin, X.; Buguin, a.; Brochard-Wyart, F. Vibrated Sessile Drops: Transition between Pinned and Mobile Contact Line Oscillations. *European Physical Journal E* **2004**, *14* (4), 395–404. https://doi.org/10.1140/epje/i2004-10021-5.

(112) Chang, C. T.; Bostwick, J. B.; Steen, P. H.; Daniel, S. Substrate Constraint Modifies the Rayleigh Spectrum of Vibrating Sessile Drops. *Phys Rev E Stat Nonlin Soft Matter Phys* **2013**, *88* (2), 1–17. https://doi.org/10.1103/PhysRevE.88.023015.

(113) Chang, C.; Bostwick, J. B.; Daniel, S.; Steen, P. H. Dynamics of Sessile Drops. Part 2. Experiment. *J Fluid Mech* **2015**, *768*, 442–467. https://doi.org/10.1017/jfm.2015.99.

(114) Miraghaie, R.; Sterling, J.; Nadim, A. Shape Oscillation and Internal Mixing in Sessile Liquid Drops Using Electrowetting-on-Dielectric (EWOD). *Technical Proceedings of the 2006 NSTI Nanotechnology Conference and Trade Show* **2006**, *2*, 610–613.

(115) Sen, P.; Kim, C.-J. Capillary Spreading Dynamics of Electrowetted Sessile Droplets in Air. *Langmuir* **2009**, *25* (8), 4302–4305. https://doi.org/10.1021/la900077u.

(116) Ko, S. H.; Lee, S. J.; Kang, K. H. A Synthetic Jet Produced by Electrowetting-Driven Bubble Oscillations in Aqueous Solution. *Appl Phys Lett* **2009**, *94* (19), 32–35. https://doi.org/10.1063/1.3123165.

(117) Mampallil, D.; Burak Eral, H.; Staicu, A.; Mugele, F.; Van Den Ende, D. Electrowetting-Driven Oscillating Drops Sandwiched between Two Substrates. *Phys Rev E Stat Nonlin Soft Matter Phys* **2013**, *88* (5), 1–8. https://doi.org/10.1103/PhysRevE.88.053015.

(118) Lathia, R.; Sagar, N.; Sen, P. Multi-Droplets Non-Coalescence on Open-Chip Electrowetting Platform. *The European Physical Journal Special Topics 2022* **2022**, 1–7. https://doi.org/10.1140/EPJS/S11734-022-00661-Z.

(119) Sagar, N.; Bansal, S.; Sen, P. Open-Chip Droplet Splitting in Electrowetting. *Adv Mater Interfaces* **2022**, *9* (28), 2200240. https://doi.org/10.1002/ADMI.202200240.

(120) Bansal, S.; Sen, P. Frequency Response of a Liquid Interface Segment Actuated Using AC EWOD. *2016 3rd International Conference on Emerging Electronics, ICEE 2016* **2017**. https://doi.org/10.1109/ICEMELEC.2016.8074591.

(121) Zhang, A.; Zha, Y.; Fu, X. Splitting a Droplet with Oil Encapsulation Using Surface Acoustic Wave Excited by Electric Signal with Low Power. *AIP Adv* **2013**, *3* (7), 072119. https://doi.org/10.1063/1.4816464.

(122) Zhang, Y.; Nguyen, N. T. Magnetic Digital Microfluidics – a Review. *Lab Chip* **2017**, *17* (6), 994–1008. https://doi.org/10.1039/C7LC00025A.

(123) Geng, H.; Feng, J.; Stabryla, L. M.; Cho, S. K. Dielectrowetting Manipulation for Digital Microfluidics: Creating, Transporting, Splitting, and Merging of Droplets. *Lab Chip* **2017**, *17* (6), 1060–1068. https://doi.org/10.1039/C7LC00006E.

(124) Zhang, K.; Xing, F.; Liu, J.; Xie, Z. Flexible On-Chip Droplet Generation, Switching and Splitting via Controllable Hydrodynamics. *Anal Chim Acta* **2022**, *1229*, 340363. https://doi.org/10.1016/J.ACA.2022.340363.

(125) Bird, J. C.; Dhiman, R.; Kwon, H. M.; Varanasi, K. K. Reducing the Contact Time of a Bouncing Drop. *Nature* **2013**, *503* (7476), 385–388. https://doi.org/10.1038/nature12740.

(126) Wang, B.; Chan, K. F.; Ji, F.; Wang, Q.; Chiu, P. W. Y.; Guo, Z.; Zhang, L. On-Demand Coalescence and Splitting of Liquid Marbles and Their Bioapplications. *Advanced Science* **2019**, *6* (10), 1802033. https://doi.org/10.1002/advs.201802033.

(127) He, P.; Kim, H.; Luo, D.; Marquez, M.; Cheng, Z. Low-Frequency Ac Electro-Flow-Focusing Microfluidic Emulsification. *Appl Phys Lett* **2010**, *96* (17), 174103. https://doi.org/10.1063/1.3424791.

(128) Yeh, C. H.; Lee, M. H.; Lin, Y. C. Using an Electro-Spraying Microfluidic Chip to Produce Uniform Emulsions under a Direct-Current Electric Field. *Microfluid Nanofluidics* **2012**, *12* (1–4), 475–484. https://doi.org/10.1007/S10404-011-0889-Z/FIGURES/8.

(129) Park, S. Y.; Wu, T. H.; Chen, Y.; Teitell, M. A.; Chiou, P. Y. High-Speed Droplet Generation on Demand Driven by Pulse Laser-Induced Cavitation. *Lab Chip* **2011**, *11* (6), 1010–1012. https://doi.org/10.1039/C0LC00555J.

(130) Collins, D. J.; Alan, T.; Helmerson, K.; Neild, A. Surface Acoustic Waves for On-Demand Production of Picoliter Droplets and Particle Encapsulation. *Lab Chip* **2013**, *13* (16), 3225–3231. https://doi.org/10.1039/C3LC50372K.

(131) Brenker, J. C.; Collins, D. J.; van Phan, H.; Alan, T.; Neild, A. On-Chip Droplet Production Regimes Using Surface Acoustic Waves. *Lab Chip* **2016**, *16* (9), 1675–1683. https://doi.org/10.1039/C5LC01341K.

(132) Ang, K. M.; Yeo, L. Y.; Friend, J. R.; Hung, Y. M.; Tan, M. K. Nozzleless Spray Cooling Using Surface Acoustic Waves. *J Aerosol Sci* **2015**, *79*, 48–60. https://doi.org/10.1016/J.JAEROSCI.2014.10.004.

(133) Yan, Q.; Xuan, S.; Ruan, X.; Wu, J.; Gong, X. Magnetically Controllable Generation of Ferrofluid Droplets. *Microfluid Nanofluidics* **2015**, *19* (6), 1377–1384. https://doi.org/10.1007/S10404-015-1652-7/FIGURES/7.

(134) Wu, Y.; Fu, T.; Ma, Y.; Li, H. Z. Ferrofluid Droplet Formation and Breakup Dynamics in a Microfluidic Flow-Focusing Device. *Soft Matter* **2013**, *9* (41), 9792–9798. https://doi.org/10.1039/C3SM51860D.

(135) Zhao, H.; Deng, Q.; Huang, T.; Zhu, P.; Li, W.; Han, X.; Li, X.; Wang, L.; Yu, P. Magnetic Field-Assisted Fission of a Ferrofluid Droplet for Large-Scale Droplet Generation. *Langmuir* **2022**. https://doi.org/10.1021/ACS.LANGMUIR.2C00437/ASSET/IMAGES/MEDIUM/LA2C00437_M018.GIF.

(136) Zaremba, D.; Błoński, S.; Korczyk, P. M. Integration of Capillary–Hydrodynamic Logic Circuitries for Built-in Control over Multiple Droplets in Microfluidic Networks. *Lab Chip* **2021**, *21* (9), 1771–1778. https://doi.org/10.1039/D0LC00900H.

(137) Li, M.; van Zee, M.; Goda, K.; di Carlo, D. Size-Based Sorting of Hydrogel Droplets Using Inertial Microfluidics. *Lab Chip* **2018**, *18* (17), 2575–2582. https://doi.org/10.1039/C8LC00568K.

(138) Chowdhury, I. U.; Sinha Mahapatra, P.; Sen, A. K. Self-Driven Droplet Transport: Effect of Wettability Gradient and Confinement. *Physics of Fluids* **2019**, *31* (4), 042111. https://doi.org/10.1063/1.5088562.

(139) Launay, G.; Sadullah, M. S.; McHale, G.; Ledesma-Aguilar, R.; Kusumaatmaja, H.; Wells, G. G. Self-Propelled Droplet Transport on Shaped-Liquid Surfaces. *Scientific Reports 2020 10:1* **2020**, *10* (1), 1–8. https://doi.org/10.1038/s41598-020-70988-x.

(140) Aliabadi, M.; Konrad, W.; Stegmaier, T.; Liu, Y.; Zhan, B.; Wang, G.; Kaya, C.; Gresser, G. Modeling of Self-Driven Directional Movement of Underwater Oil Droplets on Bio-Inspired Nano-Coated 3D-Printed Conical Models. *Sep Purif Technol* **2023**, *305*, 122405. https://doi.org/10.1016/J.SEPPUR.2022.122405.

(141) Link, D. R.; Grasland-Mongrain, E.; Duri, A.; Sarrazin, F.; Cheng, Z.; Cristobal, G.; Marquez, M.; Weitz, D. A.; Link, D. R.; Grasland-Mongrain, E.; Duri, A.; Sarrazin, F.; Cheng, Z.; Cristobal, G.; Weitz, D. A.; Marquez, M. Electric Control of Droplets in Microfluidic Devices. *Angewandte Chemie International Edition* **2006**, *45* (16), 2556–2560. https://doi.org/10.1002/ANIE.200503540.

(142) Esseling, M.; Zaltron, A.; Horn, W.; Denz, C. Optofluidic Droplet Router. *Laser Photon Rev* **2015**, *9* (1), 98–104. https://doi.org/10.1002/LPOR.201400133.

(143) Tsuchiya, H.; Okochi, M.; Nagao, N.; Shikida, M.; Honda, H. On-Chip Polymerase Chain Reaction Microdevice Employing a Magnetic Droplet-Manipulation System. *Sens Actuators B Chem* **2008**, *130* (2), 583–588. https://doi.org/10.1016/J.SNB.2007.10.014.

(144) Khalil, K. S.; Mahmoudi, S. R.; Abu-Dheir, N.; Varanasi, K. K. Active Surfaces: Ferrofluid-Impregnated Surfaces for Active Manipulation of Droplets. *Appl Phys Lett* **2014**, *105* (4), 041604. https://doi.org/10.1063/1.4891439/1.4891439.MM.ORIGINAL.V2.MOV.

(145) Jin, J.; Ooi, C. H.; Dao, D. V.; Nguyen, N. T. Liquid Marble Coalescence: Via Vertical Collision. *Soft Matter* **2018**, *14* (20), 4160–4168. https://doi.org/10.1039/c8sm00121a.

(146) Subramaniam, A. B.; Abkarian, M.; Stone, H. A. Controlled Assembly of Jammed Colloidal Shells on Fluid Droplets. *Nat Mater* **2005**, *4* (7), 553–556. https://doi.org/10.1038/nmat1412.

(147) Pan, K. L.; Tseng, Y. H.; Chen, J. C.; Huang, K. L.; Wang, C. H.; Lai, M. C. Controlling Droplet Bouncing and Coalescence with Surfactant. *J Fluid Mech* **2016**, *799*, 603–636. https://doi.org/10.1017/JFM.2016.381.

TOC Graphic:
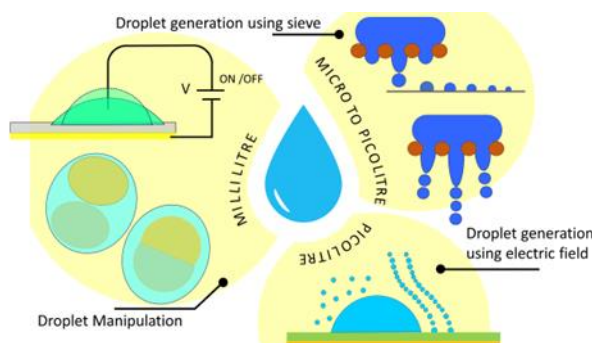
Author Information

Rutvik Lathia:

Rutvik Lathia is currently a Ph.D. student at the Centre for Nano Science & Engineering (CeNSE), Indian Institute of Science (IISc), Bengaluru, India, since 2019. Prior to joining IISc, he completed his Bachelor of Engineering (B.Tech) in Mechanical Engineering from Charotar University, Gujarat, India. He is a recipient of a Prime Minister's Research Fellowship (PMRF) during his Ph.D. tenure. His research interest includes Liquid marbles, Droplet dynamics, Microfluidics, Particle coated interfaces, and Nano-structured surfaces.

Krishnadas Narayanan Nampoothiri:

Dr. Krishnadas Narayanan Nampoothiri is currently working as an Assistant Professor (Senior Grade) at the Amrita School of Engineering Chennai campus. Before joining the institute, Krishnadas worked as a postdoctoral fellow with the National Postdoctoral Fellowship at the Indian Institute of Technology Madras, India. He has also worked as a fellow postdoc at Kansas State University for a few months and as a research associate at the Indian Institute of Science, India. He received his Ph.D. degree from the Centre for Nano Science and Engineering (CeNSE) department at the Indian Institute of Science, India, in 2020. He received his M.Tech. degree in Nano Science and Technology (2013) and B. Tech degree in Mechanical Engineering (2009) from the National Institute of Technology Calicut and Mahatma Gandhi University, respectively. University, India, in 2009. His research expertise includes microfluidics, acoustofluidics, fluid mechanics, and heat transfer.

Nitish Sagar:

Nitish Sagar is a doctoral student at the Centre for Nano Science and Engineering, Indian Institute of Science, Bengaluru, India, since 2017. His doctoral work is related to digital microfluidics platform development for lab-on-chip applications. He obtained a Master of Technology (Specialization: Thermal Engineering) from the Indian Institute of Technology (Indian School of Mines), Dhanbad, India, in the year 2017 and a Bachelor of Engineering (B.E.) degree from the Department of Mechanical Engineering, PES Institute of Technology, Bengaluru, India in the year 2015. His research interest includes (but not limited to) microfluidics, droplet-based devices, wearable devices for continuous health monitoring, and machine learning-assisted platforms.

Shubhi Bansal:

Shubhi Bansal is currently a postdoctoral research fellow at University College London, UK. She received her Ph.D. degree along with an M.Sc. (Engineering) Degree from the Centre for Nano Science and Engineering (CeNSE) department at the Indian Institute of Science, India in 2018. She received her B.Tech. degree in Engineering Physics (with a Major in Electronics and a Minor in Material Science and Technology) from Delhi Technological University, India, in 2013. She was a Research Associate at the Indian Institute of Science, India, from Aug 2018-Jan 2019. She subsequently worked as a postdoctoral research fellow with Interact lab at the University of Sussex, Falmer, UK, from 2019-2020.

Chandantaru Dey Modak:

Dr. Chandantaru Dey Modak is currently working as a Postdoctoral Researcher at Institut Pierre-Gilles de Gennes, ESPCI-PSL Paris, France. He received his Ph.D. degree from the Centre for Nano Science and Engineering (CeNSE) department at the Indian Institute of Science, India, in 2022. He received his M.Tech. degree (2017) and B.Tech degree (2014) in Chemical Engineering from the Indian Institute of Technology (Indian School of Mines), Dhanbad, and Birsa Institute of Technology, Sindri, respectively. His research interests include liquid-solid interaction, superhydrophobicity, heat engineering, drop generation techniques, and microfluidic devices for organ-on-chip applications.

Prosenjit Sen:

Prof. Prosenjit Sen received the Ph.D. degree in mechanical engineering from the University of California, Los Angeles (UCLA), in 2007, and the B.Tech. degree in manufacturing science and engineering from the Indian Institute of Technology, Kharagpur, India, in 2000. At the Micro and Nano Manufacturing Laboratory, UCLA, his research interests included microfluidic systems, droplet dynamics, liquid-metal-based RF microelectromechanical systems, and reliability of electrowetting-on-dielectric devices. From 2010-2013 he worked at Innovative Micro Technology, Santa Barbara, CA as a process engineer and program manager. Currently he is an Associate Professor in Centre for Nano Science and Engineering at Indian Institute of Science. His group works towards development of microfluidic devices and heterogeneous systems.